Article

Developmental Cell

3D Culture Method for Alzheimer's Disease Modeling Reveals Interleukin-4 Rescues Aβ42-Induced Loss of Human Neural Stem Cell Plasticity

Graphical Abstract

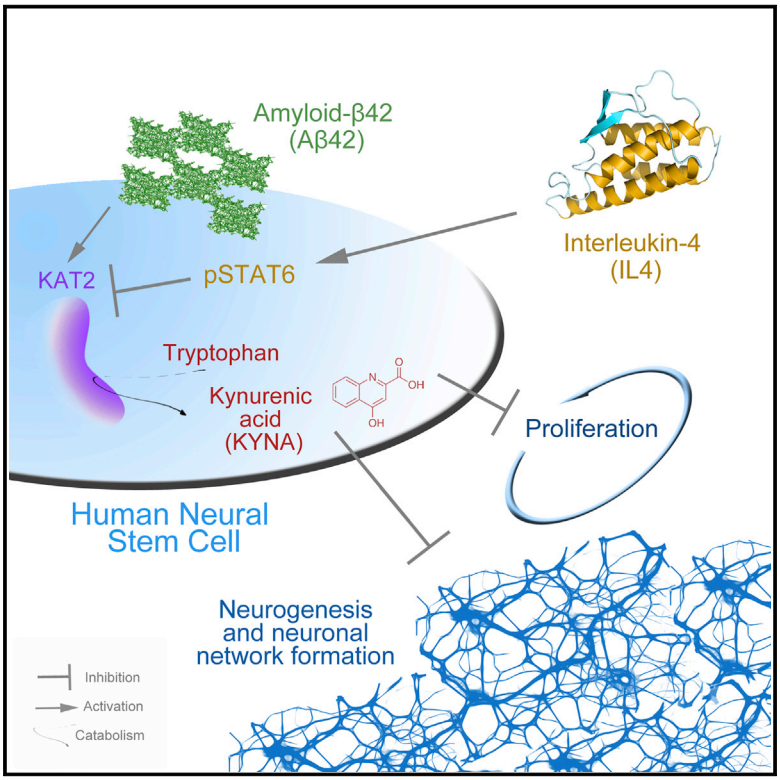

Authors

Christos Papadimitriou, Hilal Celikkaya, Mehmet I. Cosacak, ..., Uwe Freudenberg, Carsten Werner, Caghan Kizil

Correspondence

caghan.kizil@dzne.de

In Brief

Papadimitriou et al. developed a starPEG-heparin-based hydrogel 3D neuro-microenvironment that promotes human neural stem cell proliferative and neurogenic capacity. Using the system to model Alzheimer's disease (AD) uncovered kynurenic acid/IL-4 interplay, which is also observed in AD mouse and human brains, suggesting its utility for reductionist investigation of AD therapeutic targets.

Highlights

- Human neural stem cell plasticity and AD are modeled in 3D culture
- KAT2 enzyme, but not IL-4, increases in 3D culture and mouse and human brains with AD
- Aβ42-induced production of KYNA suppresses plasticity of human neural stem cells
- IL-4 antagonizes KYNA production and loss of human neural stem cell plasticity in AD

Papadimitriou et al., 2018, Developmental Cell *46*, 85–101
July 2, 2018
https://doi.org/10.1016/j.devcel.2018.06.005

CellPress

Developmental Cell
Article

3D Culture Method for Alzheimer's Disease Modeling Reveals Interleukin-4 Rescues Aβ42-Induced Loss of Human Neural Stem Cell Plasticity

Christos Papadimitriou,[1,2] Hilal Celikkaya,[1,2,9] Mehmet I. Cosacak,[1,2,9] Violeta Mashkaryan,[1,2,9] Laura Bray,[3,4] Prabesh Bhattarai,[1,2] Kerstin Brandt,[1,2] Heike Hollak,[1,2] Xin Chen,[5] Shuijin He,[5] Christopher L. Antos,[5,6] Weilin Lin,[7] Alvin Kuriakose Thomas,[7] Andreas Dahl,[2] Thomas Kurth,[2] Jens Friedrichs,[2,3] Yixin Zhang,[7] Uwe Freudenberg,[2,3] Carsten Werner,[2,3] and Caghan Kizil[1,2,8,10,*]

[1]German Center for Neurodegenerative Diseases (DZNE) Dresden, Helmholtz Association, Arnoldstr. 18, 01307 Dresden, Germany
[2]Center for Regenerative Therapies (CRTD), Technische Universität Dresden, Fetscherstr. 105, 01307 Dresden, Germany
[3]Leibniz Institute of Polymer Research Dresden, Max Bergmann Center of Biomaterials Dresden, Hohe Str. 6, 01069 Dresden, Germany
[4]Institute of Health Biomedical Innovation (IHBI), Queensland University of Technology, 60 Musk Avenue, Kelvin Grove 4059, Australia
[5]School of Life Sciences and Technology, ShanghaiTech University, Shanghai 201210, People's Republic of China
[6]Institut für Pharmakologie und Toxikologie, Technische Universität Dresden Medizinische Fakultät, Fetscherstr. 74, 01307 Dresden, Germany
[7]B CUBE, Center for Molecular Bioengineering, TU Dresden, Arnoldstr. 18, 10307 Dresden, Germany
[8]Twitter: @CaKizil and @Kizil_Lab_DZNE
[9]These authors contributed equally
[10]Lead Contact
*Correspondence: caghan.kizil@dzne.de
https://doi.org/10.1016/j.devcel.2018.06.005

SUMMARY

Neural stem cells (NSCs) constitute an endogenous reservoir for neurons that could potentially be harnessed for regenerative therapies in disease contexts such as neurodegeneration. However, in Alzheimer's disease (AD), NSCs lose plasticity and thus possible regenerative capacity. We investigate how NSCs lose their plasticity in AD by using starPEG-heparin-based hydrogels to establish a reductionist 3D cell-instructive neuro-microenvironment that promotes the proliferative and neurogenic ability of primary and induced human NSCs. We find that administration of AD-associated Amyloid-β42 causes classical neuropathology and hampers NSC plasticity by inducing kynurenic acid (KYNA) production. Interleukin-4 restores NSC proliferative and neurogenic ability by suppressing the KYNA-producing enzyme Kynurenine aminotransferase (KAT2), which is upregulated in APP/PS1dE9 mouse model of AD and in postmortem human AD brains. Thus, our culture system enables a reductionist investigation of regulation of human NSC plasticity for the identification of potential therapeutic targets for intervention in AD.

INTRODUCTION

Alzheimer's disease (AD) is a complex condition that entails profound alterations in synaptic integrity, neuronal survival, activity of the immune system, astrocyte response, and functioning of the vascular system. AD is classically characterized by loss of synaptic connections and neurons in humans (Beyreuther and Masters, 1997; Blennow et al., 2006; Ittner and Gotz, 2011; Selkoe, 2002). However, in recent years, the cellular changes and possible causes of AD are becoming more multifaceted, including chronic immune reaction, imbalance in circuit dynamics, astrogliosis, excitotoxicity, myelin breakdown, impaired neurovascular unit, and reduced neurogenic ability (De Strooper and Karran, 2016; Huang and Mucke, 2012). These phenotypic outcomes indicate that the AD pathology is a grift outcome of malfunctions in many cell types, including astrocytes, neurons, immune cells, and vasculature. According to the classical Amyloid hypothesis, Amyloid-beta42 (Aβ42) deposition and neurofibrillary tangles are two major hallmark pathologies in AD (Bertram et al., 2010; Haass and Selkoe, 2007). In recent years, it is becoming more evident that in AD pathology the neuronal proteopathy might be an endpoint and several non-neuronal changes could precede the onset of the disease in neurons. Therefore, it is important to elucidate the effects of pathological Amyloidosis in individual non-neuronal cells.

Astrocytes are of particular importance in AD. As NSCs are of astrocyte lineage in adult neurogenesis zones, astrocytes are vital for regenerative capacity by being the endogenous reservoirs of new neurons (Alvarez-Buylla et al., 2002; Doetsch, 2003; Doetsch et al., 1999; Kriegstein and Alvarez-Buylla, 2009; Laywell et al., 2000; Magnusson and Frisen, 2016). NSCs and their neuroblast lineage can divert their classical migratory routes and developmental programs to produce neurons outside their classical progeny (Arvidsson et al., 2002; Gregoire et al., 2015; Lindvall et al., 2004; Sundholm-Peters et al., 2005). Parenchymal astrocytes constitute an abundant cell type that accumulates in diseased or injured brain, and have the intrinsic property of generating neurons during embryonic development (Ahn and Joyner, 2005; Doetsch, 2003; Kriegstein and Alvarez-Buylla, 2009; Laywell et al., 2000), in disease conditions (Costa et al.,

2010; Luzzati et al., 2014; Magnusson and Frisen, 2016; Magnusson et al., 2014; Robel et al., 2011) and when reprogrammed *in vivo* (Heinrich et al., 2010; Karow et al., 2012). Parenchymal astrocytes develop from NSCs in corticogenesis (Alvarez-Buylla et al., 2002; Hansen et al., 2010; Kriegstein and Alvarez-Buylla, 2009; Molyneaux et al., 2007) and the glial scar-forming astrocytes emanate from adult subventricular zone NSCs (Faiz et al., 2015). Additionally, all embryonic astrocytes regardless of their location in the brain have the ability to form neurospheres (Laywell et al., 2000) or can form neurons when transplanted into non-neurogenic regions (Lim et al., 2009; Temple, 2001). These studies suggest that NSCs and parenchymal astrocytes are both therapeutically relevant cell types for efforts to promote endogenous neurogenesis in AD conditions, yet the effects of functional neurogenesis in human AD brains are highly controversial.

Astrocytes are also profoundly affected by Aβ42. In mouse models of AD, NSC proliferation and neurogenesis are reduced with increasing Amyloid toxicity (Demars et al., 2010; He et al., 2013; Taupin, 2009; Tincer et al., 2016). The majority of the studies linked this suppressive effect to increased inflammation; however, the direct effects of Aβ42 on astrocytes and their neurogenic ability are understudied. Additionally, since AD entails loss of neurons in the human brains, a therapeutically intriguing and controversial question toward stem cell-based regenerative therapy in AD is whether endogenous astrocytes that have intrinsic neurogenic properties could carry the hope for replenishing the lost neurons and synaptic connections, and thereby provide an internal reservoir for regeneration (Gage and Temple, 2013; Wyss-Coray, 2016). Given that adult neurogenesis and NSC activity in human brains is quite controversial (Boldrini et al., 2018; Sorrells et al., 2018), exploring the ways to modulate the NSC plasticity in disease-related settings is critical to determine if an NSC could regain proliferative and neurogenic function despite prevalent proteopathy in the brain, and whether such a neurogenic restoration could prevent or ameliorate clinical symptoms of AD. Thus, it is fundamentally important to understand how cells with neurogenic capacity may contribute to neurogenesis and regeneration in AD conditions. However, although pathogenic effects of Aβ42 in neurons are well-studied (Selkoe, 2002), little is known about how Aβ42 impairs NSC plasticity, what is the involvement of neuro-immune crosstalk in these processes, and how we can restore NSC plasticity and neurogenic activity in AD. Such questions might diversify the therapeutic approaches for AD from the neuro-centric view of the disease and could open up new research avenues.

RESULTS

Generation of starPEG-Heparin Hydrogel-Based 3D Cultures for Human Fetal Primary Astrocytes

Culture conditions that drive the generation of neurons that retain a mature neuronal morphology and form synapses and 3D patterns are better suited for addressing how the entire spectrum of plasticity manifests in the human brain. In particular, the modulation of mechanical cues, the degradability of the matrix, and the administration of soluble effectors is known to control stem cell fate (Discher et al., 2009). In this study, to generate a system that would allow neural progenitor cells to manifest their plasticity and neurogenic capacity in a tissue-representative manner, we applied a modular biohybrid material based on star-shaped poly(ethylene glycol) (starPEG) and GAG heparin (HEP) that can be used to independently tune mechanical cues and biomolecular functionalization (Tsurkan et al., 2013). By optimizing the physical characteristics of multiarmed poly(ethylene glycol)-(starPEG-) GAG hydrogels (Tsurkan et al., 2013) where the primary human cortical astrocytes (pHAs) were embedded (Figure 1A), we dissected the relevance of the matrix composition, stiffness, and susceptibility for cell-mediated remodeling for the formation of 3D neuronal networks. We showed that gels containing fully sulfated heparin, exhibiting a Young's modulus of 1.2 kPa and exposing matrix metalloproteinase cleavage sites, maximize the neurogenic potential of pHAs (Figures 1B–1F, cells expressing glial fibrillary acidic protein (GFAP) and acetylated tubulin at the same time are astroglia on their way to differentiation into neurons [Figures 1C'–1E']). We found that these initial matrix parameters effectively supported a dynamic, cell-driven generation of soft (0.3 kPa), fibronectin- and laminin-rich (Figures 1G–1J) neuro-microenvironments possessing physicochemical properties similar to the human brain (Figure 1K) (Weickenmeier et al., 2016). The formation of neurons with connected processes in 3D as opposed to 2D (Figures S1A–S1C) in the introduced assay yielded in neuronal networks with interspersed glial cells (Figure 1L). One week after seeding, the gel-based cultures contained scarcely distributed GFAP-positive glia with a 3D arborized morphology (Figure 1M). At 2 weeks, neurons form and organize into clusters (Figure 1N). After 3 weeks, the cultures produced an elaborate network of neurons with interspersed glia (Figures 1O and 1P). The gel supported the glia that expressed NSC markers SOX2 and GFAP, and the neural fate determinant NEUROD (Figures 1Q–1R3) in a 3D compartmentalized manner (Figures S1D–S1F). We could not observe such elaborate neuronal networks and patterning with using Matrigel (Figures S1G–S1L). Based on expression analyses of cell type markers, we found that 3D cultures mainly contain astrocytes and neural progenitors (Figure S1M), and our results suggest that starPEG-heparin hydrogels provide a neuro-microenvironment for manifesting neurogenic plasticity and neuronal network formation.

Comparison of 2D and 3D Culture Conditions

We hypothesized that 3D cultures would provide a 3D topological environment to pHAs and would instruct a gene expression profile that would be closer to *in vivo* than 2D cultures. To investigate how 3D cultures would molecularly differ from 2D cultures, we cultured pHAs in 2D and 3D using identical conditions. After whole transcriptome sequencing, we observed that a considerable number of genes are differentially expressed between 2D and 3D (Figure 2A, Data S1A). To identify the pathways and molecular programs represented better in 3D cultures, we performed pathway and enrichment analyses (Figure 2B). Three-dimensional cultures expressed genes related to several pathways that characterize mature neuronal physiology, such as focal adhesion, extracellular matrix (ECM)-receptor interaction, axon guidance, and various signaling pathways (Figure 2B, Data S1B). In addition, cellular component analyses indicated that 3D cultures express the genes related to various mature neuronal processes, such as synapses and axons (Figure 2B).

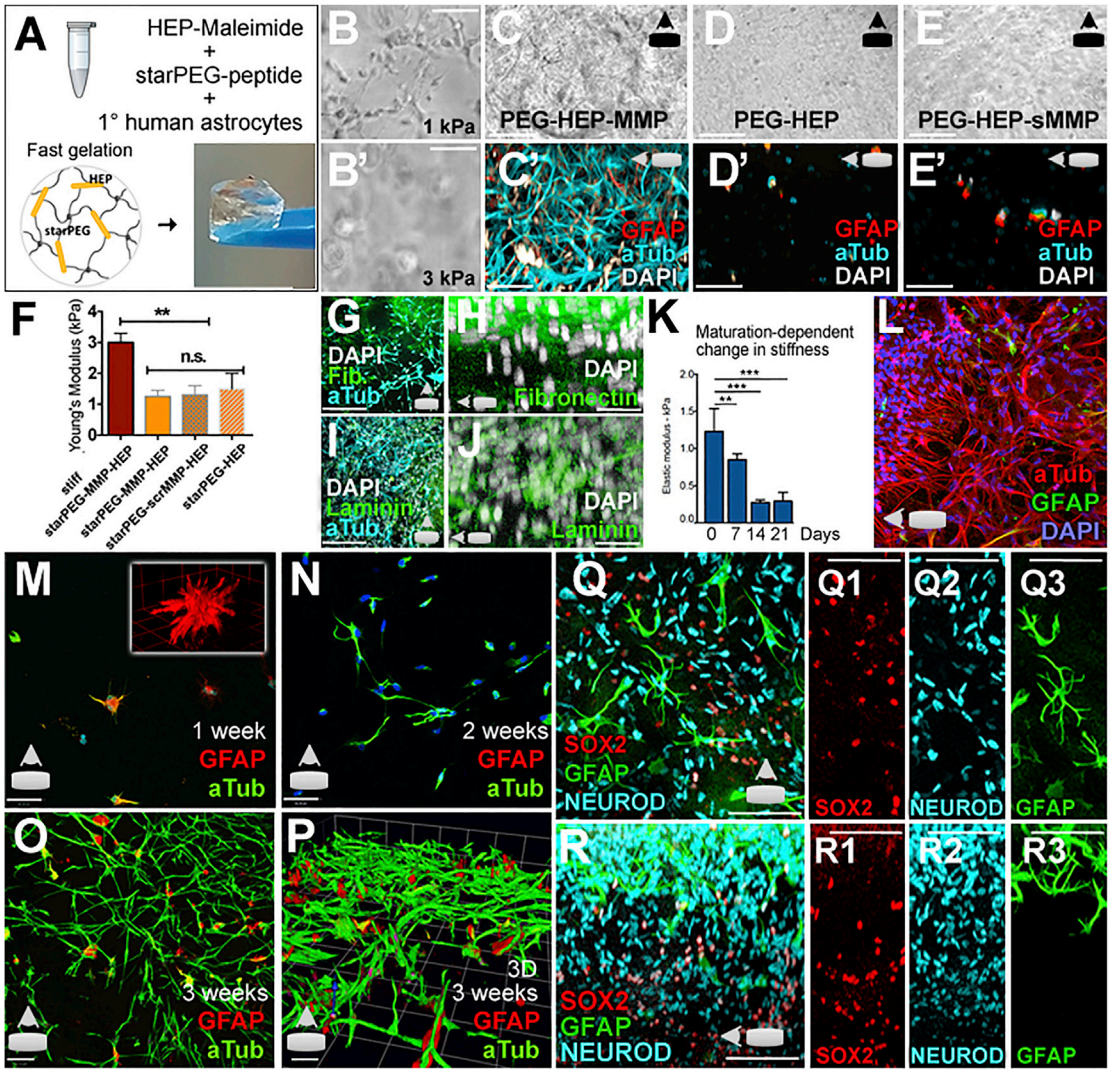

Figure 1. Physical Properties and Dynamic Remodeling of 3D starPEG-Heparin Hydrogels and Neurogenic Dynamics of Primary Human Astrocytes

(A) Simplified composition and preparation scheme of glycosaminoglycan (GAG)-based minimalist multifunctional hydrogels.

(B and B′) Bright field gel image (BFI) at 1-kPa (B) and 3-kPa (B′) stiffness.

(C–E′) BFI (C, D, and E) and immunostaining for acetylated tubulin (aTub) and GFAP (C′, D′, and E′) in a 3-week-old gel at 1 kPa stiffness with (C and C′), without (D and D′), and with scrambled MMP cleavage sites (E and E′).

(F) Rheological measurements of various gel types.

(G) Acetylated tubulin and fibronectin.

(H) Fibronectin.

(I) Acetylated tubulin and laminin.

(J) Laminin.

(K) Atomic force microscopy-based quantification of elastic modulus in the development of the neural networks.

(L) Maximum projection for TUBB3 and GFAP (x axis).

(M–O) Acetylated tubulin/GFAP staining over the *z* axis after 1 (M), 2 (N), and 3 (O) weeks of culture.

(P) 3D representation for acetylated tubulin and GFAP.

(Q–R3) Maximum projection images for SOX2, GFAP, and NEUROD1 over the z axis (Q–Q3) and x axis (R–R3). Single fluorescent channels are shown on the right (Q1–Q3, R1–R3).

Error bars represent the means ± standard deviations. The levels of significance are $^{**}p \leq 0.01$, and $^{***}p \leq 0.001$. Scale bars, 10 μm for (H), (J), and (M)–(P); 50 μm for the other figures. Gels: 3 weeks of culture. See also Figure S1.

These results indicate that our hydrogel cultures provide the 3D topology and instructive environment to generate neuronal networks from pHAs in a tissue-mimetic manner, unlike 2D cultures.

To verify that the 3D cultures of pHA generate mature neurons resembling the *in vivo* conditions, we immunostained 3D gels for the synaptic marker synaptophysin (Figure 2C), which clusters at

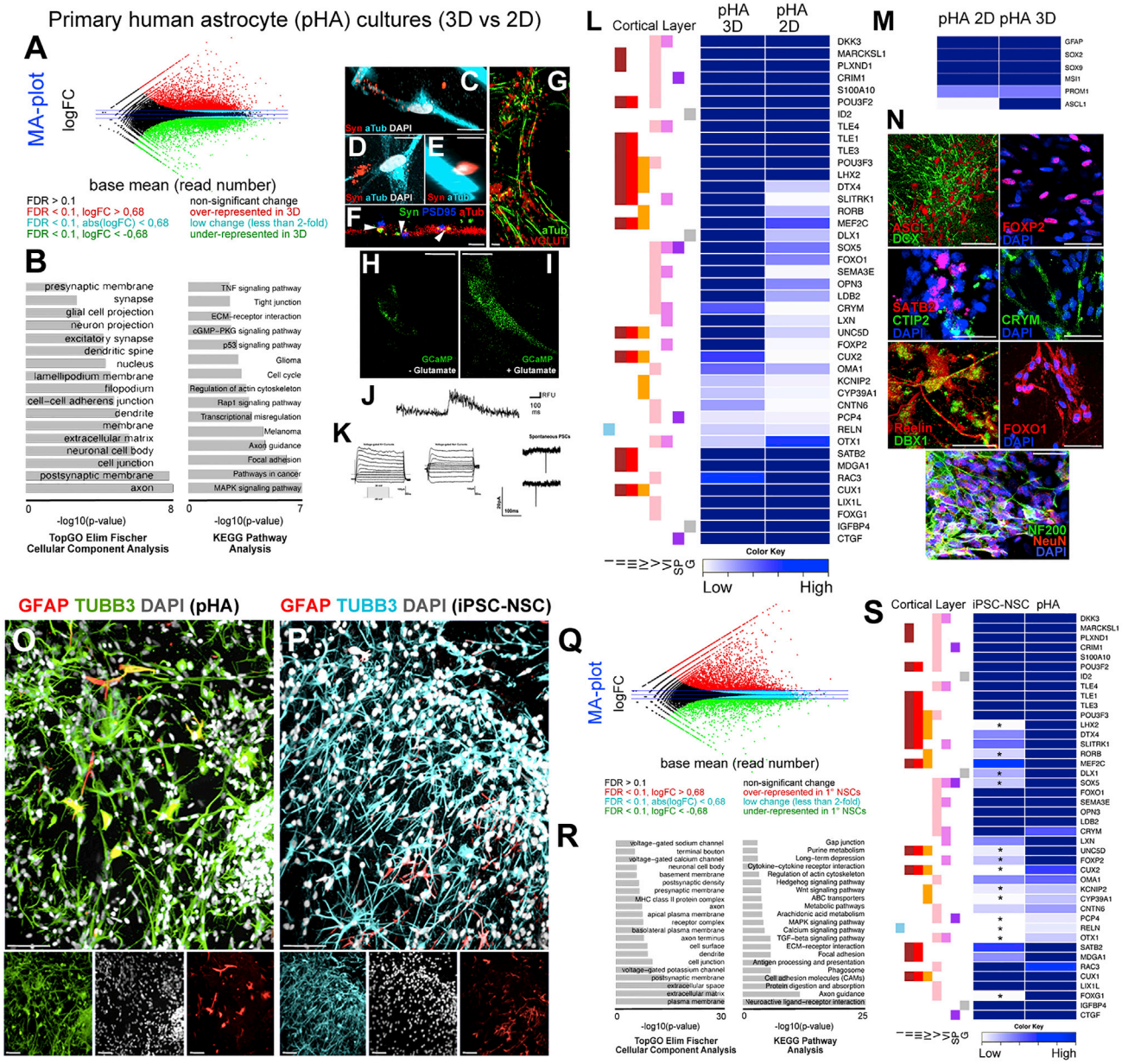

Figure 2. Comparison of Gene Expression Profiles of Primary Human Cortical Astrocytes in 2D and 3D Cultures, and iPSC-Derived NSCs in 3D

(A) MA-plot for differentially expressed genes between 3D and 2D cultures of primary human fetal astrocytes (pHA). Red, upregulated in 3D; green, downregulated in 3D.

(B) KEGG pathway analyses pie chart showing significantly enriched molecular pathways.

(C–E) Synaptophysin and acetylated tubulin immunostaining in 3D cultures.

(F) Synaptophysin, PSD95, and acetylated tubulin immunostaining in 3D cultures. Arrowheads indicate juxtaposed pre- and post-synaptic stainings.

(G) VGlut1 and acetylated tubulin immunostaining in 3D cultures.

(H) GCaMP6 signal without glutamate treatment.

(I) GCaMP6 signal with glutamate treatment.

(J) Fluorescence intensity histogram. Note the peak at the time of glutamate treatment.

(K) Patch clamp recordings for Na+ (left) and K+ (middle) currents. Detection of spontaneous firing of neurons (right).

(L) Heatmap for expression levels of cortical marker genes for 2D and 3D cultures. Genes are denoted with their respective cortical layer expression with color codes (left to the heatmap).

(M) Heatmap for expression levels of neural stem/progenitor cell markers.

(N) Immunostaining for ASCL1 (proneural determinant), DCX (early neuronal marker), SATB2, CTIP2, Reelin (RELN), DBX1, FOXP2, CRYM, FOXO1 (cortical markers), and Neurofilament (NF200) and NeuN (mature neuronal markers).

(legend continued on next page)

neuronal junctions (Figure 2D) and boutons (Figure 2E), and generates pre- and post-synaptic termini (Figure 2F), indicating that neurons in 3D cultures unlike in 2D develop enough to form synaptic connections. Neurons formed in the 3D starPEG-HEP-based hydrogels were also expressing neurotransmitter receptors such as VGlut1 (Figure 2G) and were responsive to glutamate as shown by increased intracellular calcium (Figures 2H–2J; Video S1) after GCamP6f calcium sensor expression by plasmid transfection. We also performed electrophysiology experiments assessing sodium and potassium channel activity. We observed potassium and sodium channel activity as well as spontaneous firing of neurons in whole cell patch clamp recordings (Figure 2K), indicating that cells in the hydrogels differentiated into functionally active mature neurons.

To determine the cortical subtypes produced in 3D and 2D, we compared the expression levels of a set of cortical genes in relation to their spatial confinement to different layers (Figure 2L). We observed that 3D conditions favor expression of a larger set of cortical markers compared with 2D (Figure 2L). Similarly, although 2D and 3D conditions allow expression of NSC markers, 3D cultures allow significantly higher levels of ASCL1 expression (Figure 2M), suggesting a reason why 3D conditions provide a better neurogenic ability to pHAs. Our deep sequencing results and heatmap analyses are verified by immunohistochemistry for proneural determinant ASCL1 and early neuronal marker DCX, cortical layer markers SATB2, CTIP2, Reelin (RELN), DBX1, FOXO1, FOXP2, CRYM, and mature neuronal markers Neurofilament-200 and NeuN (Figure 2N), indicating that 3D culture can be used to assay the wide spectrum of human NSC plasticity from proliferation to neuronal network formation.

Induced Pluripotent Stem Cell-Derived Neural Stem Cells in starPEG-Heparin Hydrogels

To test whether we could use our system with NSCs, we cultured induced pluripotent stem cell-derived human neural stem cells (iPSC-NSCs) in culture under conditions identical to those of pHAs, and observed extensive neurogenesis and network formation (Figures 2O and 2P; Video S2), suggesting that our instructive hydrogel composition can support development of networks from various types of NSC sources. To compare the molecular expression profiles of pHAs and iPSC-NSC cultures, we performed whole transcriptome sequencing (Figure 2Q, Data S1C). We found that although both iPSC-NSCs and pHAs can generate neuronal networks in 3D, two cell types differ significantly in gene expression patterns (Figure 2Q; Data S1D). Interestingly, compared with iPSC-NSCs, pHA cultures express genes related to ECM and plasma membrane (Figure 2R; Data S1E), and these differences enrich pathways such as signaling pathways, axon guidance, neuroactive ligand-receptor interaction and metabolism (Figure 2R; Data S1F). When we compared cortical layer marker expression in iPSC-NSCs and pHAs, we found that compared with pHAs, iPSC-NSC cultures cannot form a subset of neuronal lineages especially for layers in our particular culture conditions (Figure 2S). These findings suggest that our 3D culture system can be used to dissect the properties and neurogenic capacities of different progenitor types and may serve as a suitable tool for investigating the physiological differences between induced and primary progenitor populations.

Modeling Aβ42 Toxicity in starPEG-Heparin Hydrogels

In mouse models of AD, Aβ42 aggregation impairs neuronal connectivity (Hardy and Selkoe, 2002; Kienlen-Campard et al., 2002; LaFerla et al., 2007; Selkoe, 2002; Tincer et al., 2016) and Aβ42 was shown to negatively affect the plasticity of glial cells and neurogenesis (Ermini et al., 2008; Haughey et al., 2002; Heo et al., 2007). Although it is not clear whether neurogenesis is functionally related to AD pathology in humans, theoretically, the reduced NSC plasticity could be one of the principal limitations of neuro-regeneration in AD (Cosacak et al., 2015; Demars et al., 2010; Tincer et al., 2016). However, the mechanisms underlying the impact of Aβ42 on progenitor plasticity are still largely unknown and cannot be elucidated analytically in human brains. We therefore aimed to model impaired NSC plasticity and neurogenesis in AD by treating pHAs with Aβ42 before embedding them in the biohybrid hydrogels (Figure 3A). We used an Aβ42 form that we previously found to be causing pathological outcomes in vertebrate brains (Bhattarai et al., 2016, 2017b) and that aggregates in early endosomes (Figures S2A–S2D) leading to cell death (Figures S2E and S2F).

To test whether Aβ42 would cause pathological outcomes, we tested its effects on neuronal network formation, neuronal morphology, TAU hyperphosphorylation, neurofibrillary tangle formation, synaptic integration, progenitor cell proliferation, and neurogenesis (Figure 3). In control gels, neurons formed highly connected networks (Figure 3B) that were disrupted upon Aβ42 (Figure 3C). We developed an algorithm to trace the connected neuronal paths as skeletonized arbors and quantified the extent of the neuronal connections, and observed that neuronal networks reduce significantly after Amyloid toxicity (Figures 3D–3F). Similar to human brains, Aβ42 resulted in dystrophic axons (Figure 3G–3G''; Video S3), impaired ECM composition and stiffness (Figures 4H–4J), TAU hyperphosphorylation (Figures 3K–3N, Video S4), neurofibrillary tangle formation as observed by Gallyas silver impregnation (Figures 3M and S2) and Thioflavin S staining (Figure 3N), microtubule

(O) Immunostaining for GFAP (red) and TUBB3 (green) on 3 weeks of 3D cultures with primary human fetal cortical astrocytes. Insets below the panel are individual fluorescence channels including DAPI (white).

(P) Immunostaining for GFAP (red) and TUBB3 (cyan) on 3 weeks of 3D cultures with iPSC-derived human neural stem cells (iPSC-NSC). Insets below the panel are individual fluorescence channels including DAPI (white).

(Q) MA-plot for differentially expressed genes in pHA over iPSC-NSC cultures. Red: over-represented in primary cultures, green: underrepresented in pHA compared with iPSC-NSC cultures.

(R) KEGG pathway analyses pie chart showing significantly enriched molecular pathways in pHA compared with iPSC-NSC cultures.

(S) Heatmap for expression levels of cortical marker genes in iPSC and primary cultures. Asterisks indicate significant difference between two samples. Genes are denoted with their respective cortical layer expression with color codes (left to the heatmap).

Scale bars, 10 μm for (C)–(I); 25 μm for (N); 100 μm for (O) and (P). Gels: 3 weeks of culture. See also Videos S1 and S2, and Data S1A–S1F.

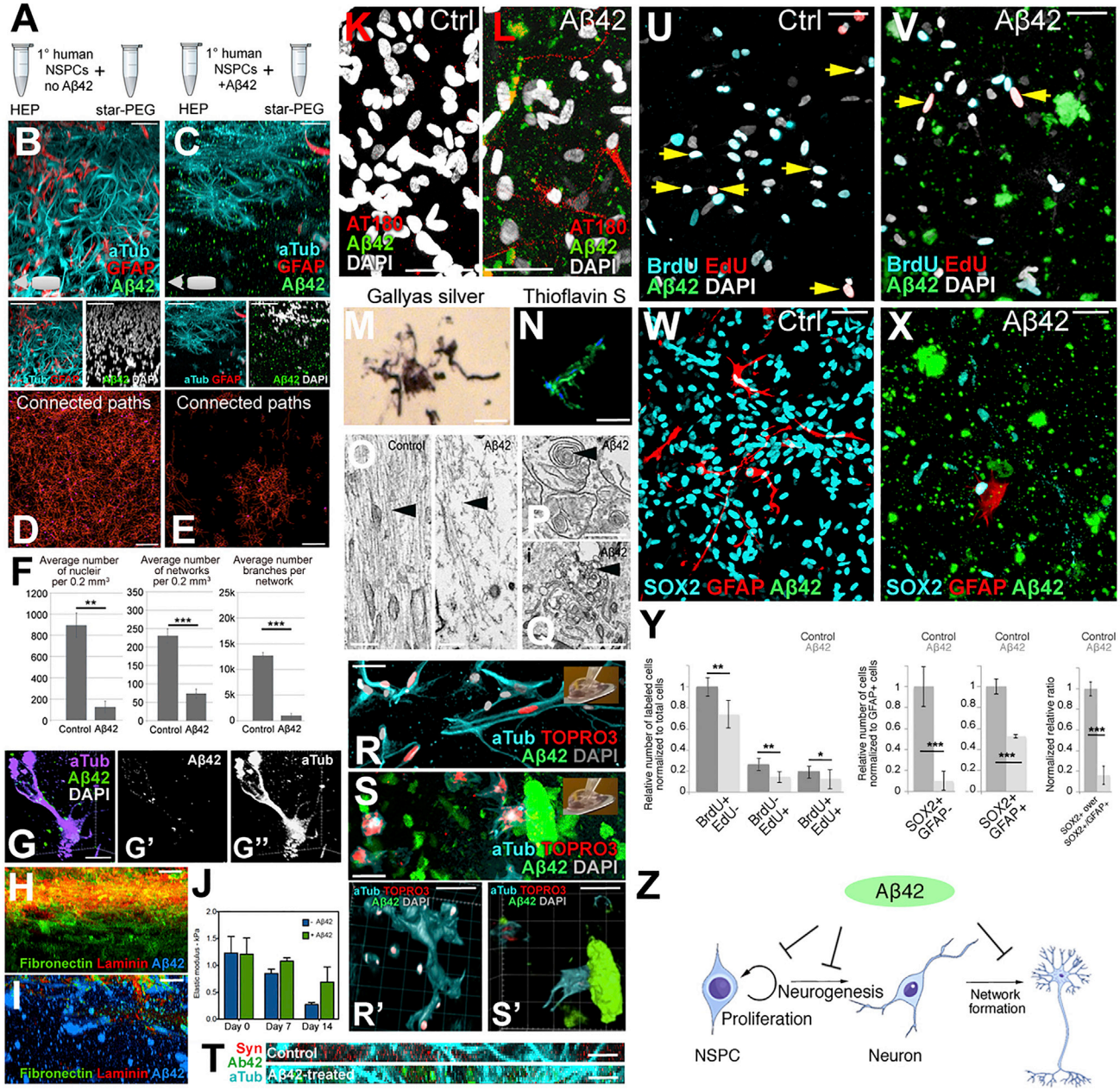

Figure 3. Aβ42 Toxicity Model in GAG-Based Hydrogel Cultures of Primary Human Fetal Astrocytes

(A) Simplified gel preparation/Aβ42 administration scheme.

(B and C) X axis views for Aβ42, acetylated tubulin, GFAP in control (B) and Aβ42 gels (C). Double stainings under the panels.

(D and E) Maximum projection of the skeletonized connected neuronal pathways in control (D) and Aβ42 gels (E).

(F) Quantification.

(G–G″) 3D-reconstruction of TUBB3/Aβ42 showing dystrophic axons.

(H and I) Fibronectin/laminin in control (H) and Aβ42 gels (I).

(J) Time course atomic force microscopy measurements of stiffness.

(K and L) Phospho-Tau (AT180) in control (K) and Aβ42 gels (L).

(M) Gallyas silver staining.

(N) Thioflavin S staining in Aβ42 gels.

(O) Electron microscopy images of microtubules in control (left) and Aβ42 gels (right). Arrowheads indicate respective regions where microtubule tracks are affected by Aβ42.

(P and Q) Aβ42 depositions indicated by arrowhead (P), and autophagic vacuoles indicated by arrowhead (Q).

(R–S′) Acetylated tubulin and Aβ42 in control (R) and Aβ42 gels (S) after transplantation. Transplanted cell nuclei labeled with TOPRO3 (red). 3D-reconstruction of R (R′) and S (S′).

(legend continued on next page)

disassembly (Figure 3O), and Amyloid aggregation and autophagy (Figures 3P and 3Q), indicating that Aβ42 can recapitulate its known toxic effects in our 3D culture conditions.

Amyloid toxicity not only impairs neurogenesis and neuronal survival, but also reduces synaptic plasticity in mouse models as Amyloid load prevents the formation of new synapses, and newly added cells cannot integrate into the circuitry, rendering exogenous stem cell therapy inefficient (Lilja et al., 2015; Tong et al., 2015). We developed a transplantation paradigm with cultured gels to test whether our 3D culture model could be used to address questions on the capacity of transplanted cells to integrate into existing networks (Figure 3R). We labeled all pHAs with a nuclear stain, and transplanted them into another hydrogel that had been pre-cultured with embedded pHAs for 1 week (Figure 3R). At 1 week after transplantation, the new cells formed neurons with arbors (red nuclei, Figure 3R; Video S5) and connected to pre-existing cells in the control gels (Figures 3R and 3R′). In contrast, the cells that were transplanted into Aβ42-containing gels did not acquire an arborized morphology or connect to the existing cells that were also not arborized (Figures 3S and 3S'; Video S6). These results suggest that our 3D cultures can be used for analyzing how synaptic connections can be regenerated and how new neurons can be forced to integrate into the existing circuitry upon Aβ42 toxicity.

Aβ42 reduces the NSC plasticity and neurogenic capacity in mouse models of AD, and stem cell-based regenerative therapies may be enabled by activation of NSCs (Tincer et al., 2016). To investigate whether Aβ42 would reduce the plasticity in our 3D cultures, we determined the proliferative capacity and prevalence of pHAs after Aβ42 by BrdU/EdU treatment and immunohistochemical stainings for NSC markers SOX2 and GFAP (Figures 3U–3X). We treated the cultures with BrdU (at 1 week) and EdU (at 2 weeks), and analyzed the presence of label-positive cells at 3 weeks where double-positive cells would indicate constitutively proliferating progenitors (Figures 3U and 3V). Aβ42 reduced BrdU-EdU incorporation and the relative normalized number of constitutively proliferating cells (Figure 3Y) as well as decreased the numbers of GFAP and SOX2-positive progenitors and their neurogenic outcome (Figure 3Y). These results indicate that our 3D culture system can be used for modeling Aβ42-induced impairment of NSC plasticity, and can also successfully serve as an *in vitro* sporadic AD model of Aβ42 toxicity on plasticity and neurogenesis (Figure 3Z).

To determine whether the effects of Aβ42 observed in our cultures are specific and not due to general protein aggregation toxicity, we have performed control experiments using Aβ38 and scrambled Aβ42 (Figures S2G–S2M). Aβ38 did not cause cellular toxicity, cell death, or reduced cell proliferation in contrast to Aβ42 (Figures S2G–S2I). We also tested the effects of Aβ42 and Aβ38 in cultured human fibroblasts and observed that neither Aβ42 nor Aβ42 causes toxicity (Figures S2J–S2L), indicating that Aβ42 toxicity is specific to nervous system cells. We used the scrambled Aβ42 peptide as documented before (Bhattarai et al., 2016, 2017a), and found that it does not exert toxicity on pHAs (Figure S2M). These findings indicate that the Aβ42 toxicity is specific.

To determine if Aβ42 would affect the neuronal network formation and NSC plasticity in iPSC-NSCs, we treated these cells with Aβ42 and encapsulated in 3D gels. To determine the neuronal network formation, NSC prevalence, and proliferative capacity, we performed immunostainings for GFAP and TUBB3 (Figures 4A and 4B), SOX2 and GFAP (Figures 4C and 4D), and GFAP and BrdU (Figures 4E and 4F) together with Aβ42 detection. Compared with controls, Aβ42 reduces the total number of newborn cells and NSCs (GFAP/SOX2) (Figure 4G), average values for number of networks (Figure 4H), number of branches per network (Figure 4I), branch length per network (Figure 4J), length of longest connected path (Figure 4K), and maximum branch length (Figure 4L) in iPSC-NSC cultures. These results show that Aβ42 impairs the plasticity, neurogenic ability, and network-forming capacity of pHAs and iPSC-NSCs in our 3D hydrogels.

Transcriptional Changes Exerted by Aβ42

To determine the gene expression changes exerted by Aβ42 in 3D cultures, we performed whole transcriptome sequencing on control and Aβ42-treated cultures with iPSC-NSCs (Figure 4M, Data S2A) and pHAs (Figure 4N, Data S2B). Cellular component analyses and Kyoto Encyclopedia of Genes and Genomes (KEGG) pathway enrichment analyses in iPSC-NSC-derived (Figure 4O, Data S2C and S2D) and pHA (Figure 4P, Data S2E and S2F) cultures showed that divergent pathways are affected by Aβ42. Hierarchical clustering (Figure 4Q) and multivariate analyses (Figure 4R) indicated that pHAs and iPSC-NSCs have their own molecular signatures of gene expression, which are affected by Aβ42. By plotting a heatmap of gene expression changes, we found that several cortical marker genes are differentially expressed after Aβ42 (Figure 4S), which is suggestive of the alterations in the cortical neuronal subtypes, which we have verified with immunohistochemical stainings (Figure 4T). Our results indicate that although Aβ42 causes impaired plasticity, neurogenesis and network formation in both iPSC-NSCs and pHAs (Figures 3 and 4), the molecular programs it alters in these cultures do differ (Figures 4O, 4P, and 4S). This finding is consistent with previous documentations that primary and induced progenitors have profound physiological differences that might affect subsequent global gene expression, neuronal maturation capacity, and resilience to disease conditions (Kim et al., 2010, 2011; Verpelli et al., 2013; Xia et al., 2016). Therefore, our results suggest that starPEG-heparin 3D culture system can also be used to dissect the effects of Aβ42 on different stem/progenitor cell and neuronal populations. Since our cultures do not contain

(T) Acetylated tubulin, synaptophysin, Aβ42 in control (upper) and Aβ42 gels (lower).
(U and V) BrdU and EdU in control (U) and Aβ42 gels (V). Arrows: double-positive cells.
(W and X) SOX2, GFAP, Aβ42 in control (W) and Aβ42 gels (X).
(Y) Quantification of (U)–(X).
(Z) Schematics for effects of Aβ42.
Error bars represent the means ± standard deviations. The levels of significance are *$p \leq 0.05$, **$p \leq 0.01$, and ***$p \leq 0.001$. Scale bars, 10 μm for (G), (M), (N), (T), (R), and (S); 200 nm for (O)–(Q); 50 μm for the other figures. Gels: 3 weeks of culture. See also Figure S2, Videos S3, S4, S5, and S6.

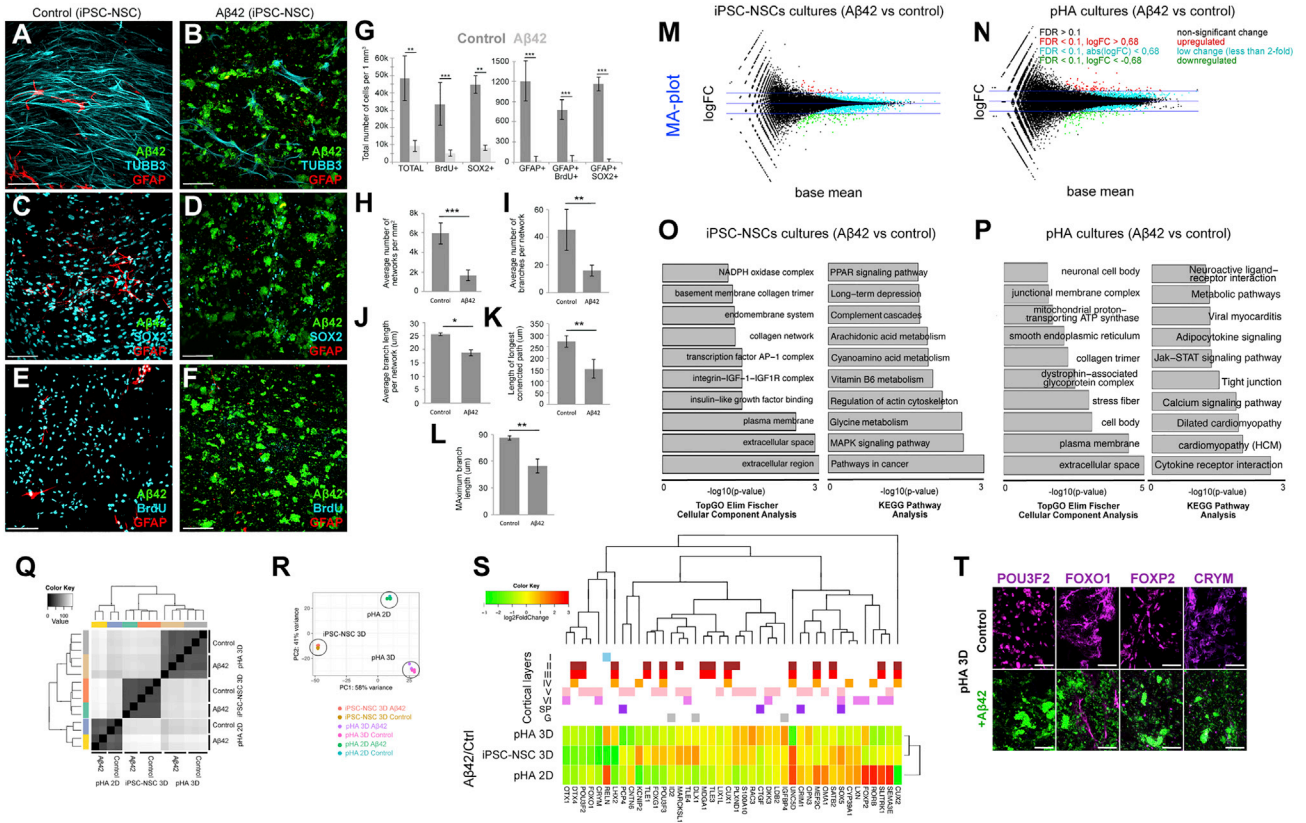

Figure 4. Aβ42 Toxicity Model with Human iPSC-Derived Neural Stem Cells (iPSC-NSC) in 3D Hydrogels, Analysis of Transcriptional Changes, and Comparison to Primary Human Fetal Astrocyte Cultures

(A) Immunostaining for Aβ42 (green), TUBB3 (cyan), and GFAP (red) on control iPSC-derived NSC (iPSC-NSCs) cultures.

(B) Immunostaining for Aβ42 (green), TUBB3 (cyan), and GFAP (red) on Aβ42-treated iPSC-NSC cultures.

(C) Immunostaining for Aβ42 (green), SOX2 (cyan), and GFAP (red) on control cultures.

(D) Immunostaining for Aβ42 (green), SOX2 (cyan), and GFAP (red) on Aβ42-treated cultures.

(E) Immunostaining for Aβ42 (green), BrdU (cyan), and GFAP (red) on control cultures. BrdU is given at 1 week of culture.

(F) Immunostaining for Aβ42 (green), TUBB3 (cyan), and GFAP (red) on Aβ42-treated cells. BrdU is given at 1 week of culture.

(G) Quantification graph for number of cells in control and Aβ42-treated cultures.

(H–L) Quantification of average number of networks (H), average number of branches per network (I), average branch length per network (J), length of longest connected path (K), and maximum branch length (L).

(M) MA-plot for differentially expressed genes in iPSC-NSC cultures after Aβ42 treatment. Red: upregulated, green: downregulated.

(N) MA-plot for differentially expressed genes in primary human fetal astrocyte (pHA) cultures after Aβ42 treatment. Red, upregulated; green, downregulated.

(O) KEGG pathway analyses pie chart showing significantly enriched molecular pathways in cultures after Aβ42 treatment.

(P) KEGG pathway analyses pie chart showing significantly enriched molecular pathways in pHA cultures after Aβ42 treatment.

(Q) Hierarchical clustering of pHA 3D, iPSC-NSC 3D, and pHA 2D samples.

(R) Multivariate analyses of gene expression datasets for pHA 3D, iPSC-NSC 3D, and pHA 2D cultures.

(S) Heatmap for changes in expression levels of cortical marker genes in iPSC-NSC and pHA cultures after Aβ42 treatment. Genes are denoted with their respective cortical layer expression with color codes (above the heatmap).

(T) Immunostainings for POU3F2, FOXP2, FOXO1, and CRYM in control and Aβ42-treated 3D pHA cultures. Reductions in expression of these markers confirm the heatmap in (S).

Error bars represent the means ± standard deviations. The levels of significance are *$p \leq 0.05$, **$p \leq 0.01$, and ***$p \leq 0.001$. Scale bars, 100 μm (A–F) and 50 μm (T). Gels: 3 weeks of culture. See also Figure S2 and Data S2A–S2F.

inflammatory cells, our method will also help to investigate the direct role of individual neuroinflammatory factors and Aβ42 on NSCs and neurons in a reductionist and dissective manner.

Interleukin-4 Rescues Aβ42-Induced Loss of NSC Plasticity and Neurogenesis

The anti-inflammatory cytokine interleukin-4 (IL-4) has previously been implicated in regulating NSC proliferation in rodent models by converting macrophages into a post-inflammatory state, suggesting an indirect negative role of inflammation on NSC plasticity (Griffin, 2013). Conversely, we have recently reported direct effects of IL-4 on NSCs in an adult zebrafish brain model of AD, suggesting a positive role for neuroinflammatory cues in neuroregeneration (Bhattarai et al., 2016). For humans, however, the direct role of IL-4 on neural progenitor plasticity and neurogenic capacity is still unknown. To address this question, we used the

biohybrid starPEG-GAG hydrogel-based cultures that are particularly well-suited to our question since the materials were previously shown to reversibly bind and protect IL-4 in ways resembling its complexation in ECMs (Schirmer et al., 2016), resulting in the effective modulation of the activity of anti-inflammatory cytokines (Freudenberg et al., 2016). We found that IL-4 receptor (IL-4R) is expressed in GFAP-positive astrocytes and can lead to phosphorylation of STAT6 after IL-4 treatment (Figures 5A–5B′), confirming functional intracellular signaling. To determine whether IL-4 treatment affects the normal development and composition of the pHA cultures, we compared the control (Figures 5C–5E) and IL-4-treated cultures (Figures 5F–5H). We observed that IL-4 does not affect the total number and composition of pHAs and neurons in starPEG-heparin 3D cultures (Figure 5I), indicating that IL-4 does not alter the plasticity and neurogenic capacity of healthy primary human astrocytes during neurodevelopment.

To determine whether IL-4 treatment would have an effect on the reduction of pHA plasticity, neurogenic properties, and network formation of the neurons, we cultured Aβ42-treated cells in the presence of IL-4 (Figures 5J–5O). Compared with controls, Aβ42 significantly reduced neurogenic pHAs (GFAP/SOX2) and early neurons (NEUROD/DCX), while IL-4 rescued this reduction (Figure 5P). Quantifying the activated (GFAP+/SOX2+) fraction of pHAs (GFAP and/or SOX2-positive cells), we found that IL-4 significantly increased the percentage of neurogenic pHAs (Figure 5Q) that manifests itself in the formation of more DCX-positive neurons and networks (Figures 5R–5R″). To validate the positive effect of IL-4 on activation of proliferation of pHAs and neurogenesis, we determined the levels of BrdU-positive newborn cells at 3 weeks of 3D cultures after a 6-hr BrdU treatment during the first week (Figure 5S–5U). We found that Aβ42 administration reduced the total number of newborn cells (~96.1%) and BrdU+ glia significantly (~86.5%), while IL-4 treatment rescued these reductions and enhanced the ratio of newborn cells to the BrdU+/GFAP+ cells (Figure 5V). These results indicate that Aβ42 impairs progenitor plasticity, neurogenic capacity, and network-formation ability of pHAs and neurons while IL-4 restores these features despite the prevalent AD toxicity (Figure 5W). We also identified that IL-4 treatment induced phosphorylation of intracellular signal transducer STAT6 in comparison with control and Aβ42-treated gels (Figure 5X). Thus, IL-4 signaling through pSTAT6 can rescue Aβ42-induced impairment of proliferation and neurogenic ability of pHAs (Figure 5Y). The rescue effect of IL-4 is specific because knocking-down IL-4 activity using a neutralizing antibody significantly reduced the rescue effect (Figure S3). Overall, these results suggest that our starPEG-heparin 3D hydrogel cultures of pHAs can recapitulate the tissue-mimetic manifestation of neurogenic capacity and plasticity and can be used to investigate the direct effects of particular immune-related factors in a reductionist manner.

Kynurenic Acid Mediates Aβ42 Toxicity and Is Suppressed by IL-4

Since our 3D cultures can be used to investigate the direct effects of IL-4, we also aimed to analyze the downstream regulation by IL-4. We previously found that IL-4 increases NSC proliferation in adult zebrafish brain after Aβ42 (Bhattarai et al., 2016). Whole-genome transcriptome analysis of this model revealed differentially expressed and enriched components of the tryptophan metabolism pathway that ultimately generated kynurenic acid (KYNA) (Bhattarai et al., 2016). While KYNA was reported to be a neuroprotective molecule (Schwarcz et al., 2012; Szalardy et al., 2012; Zwilling et al., 2011), its direct effect on NSCs is unknown (Jones et al., 2013). We hypothesized that the rescuing effects of IL-4 on Aβ42-mediated impairment of neurogenic plasticity could proceed through the regulation of the production of KYNA.

To test this hypothesis, we compared the expression of the enzymes producing KYNA through the catabolic cascade involving three enzymes: IDO1, TDO2, and KAT2 (Figures 6A–6D and S4). Although the levels of IDO1 and TDO2 increased by 3-fold after Aβ42, IL-4 cannot affect this increase (Figures S4G–S4I). However, Aβ42 increased the abundance of cells expressing KAT2 and increased the KAT2 levels significantly (Figures 6E and S5A). IL-4 restored the control KAT2 expression pattern (Figure 6D) and levels (Figure S5B), suggesting that Aβ42 toxicity on NSCs might be mediated by elevated KAT2 activity and in turn higher levels of KYNA. Therefore, we hypothesized that an effective concentration of KYNA produced in cultures should correlate with Aβ42 toxicity, and IL-4 treatment could reduce these levels. To test this hypothesis, we performed mass spectrometry coupled to liquid chromatography for detecting the levels of KYNA in cell culture medium from control, IL-4-treated, Aβ42-treated, and Aβ42 + IL-4-treated gels (Figures S5C–S5E). We found that the KYNA production was significantly increased after Aβ42 treatment and IL-4 reduces this level down to control levels (Figure 6E'). These results indicate that KYNA mediates Aβ42 toxicity in pHAs and IL-4 reduces effective KYNA concentration to physiological levels.

To investigate how KYNA affects proliferative and neurogenic properties of pHAs and whether this effect is similar to Aβ42, we performed immunocytochemical staining for GFAP and SOX2 (Figures 6F–6H). We found that KYNA reduced the total number of GFAP+, SOX2+, and GFAP/SOX2 double-positive cells similar to Aβ42 (Figure S6A) and reduced the percentage of neurogenic progenitors (GFAP+/SOX2+) (Figures 6I and S6A). Furthermore, KYNA diminished the proliferative capacity of pHAs (Figures 6J–6L and S6B–S6D).

Since IL-4 reduces the production of KYNA by suppressing the expression of KAT2, we hypothesized that blocking the KAT2 activity would mimic the effects of IL-4 on plasticity. Therefore, we inhibited KAT2 with the selective antagonist BFF12, and found that the reduction in GFAP+ and SOX2+ cells by Aβ42 is counteracted by BFF12 treatment similar to IL-4 (Figures 6M–6O). Thus, the restorative effect of KAT2 inhibition by BFF12 on the diminished pHA plasticity (GFAP/SOX2) is comparable to IL-4 treatment (Figure 6P). These results indicate that KYNA is a mediator of Aβ42 toxicity in astrocytes with neurogenic ability and Aβ42 reduces human neural progenitor proliferation and neurogenic capacity through elevated levels of KAT2-catalyzed KYNA, which is suppressed by IL-4 (Figure 6Q).

We further hypothesized that if IL-4 can restore the plasticity and neurogenic output of pHAs upon Aβ42 toxicity mediated by KYNA, the expression of stem cell and cortical neuron markers should change similarly in Aβ42 and KYNA-treated gels, and IL-4 should restore those expression levels. After

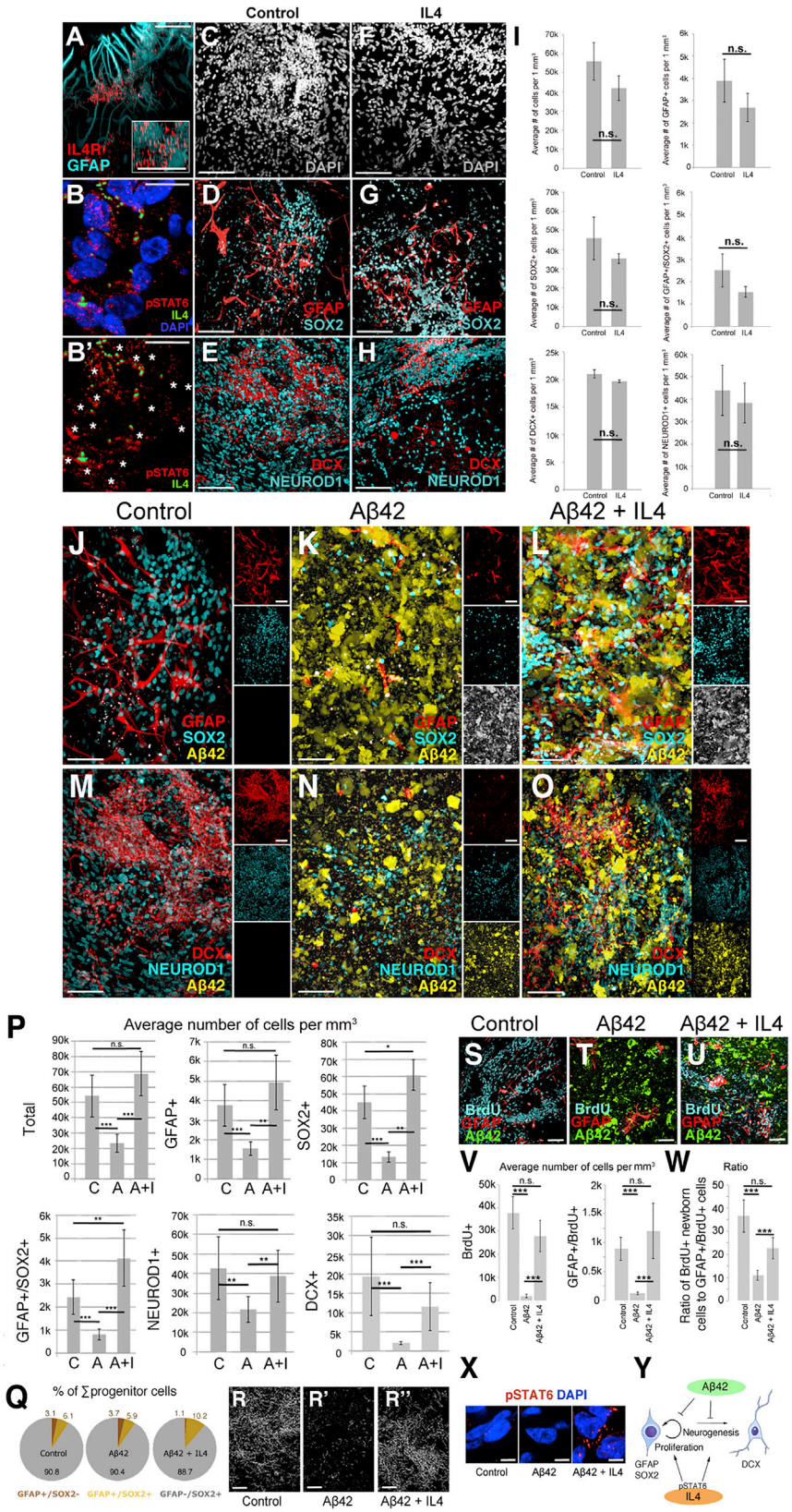

Figure 5. Effects of IL-4 on 3D Cultures of Primary Human Fetal Cortical Astrocytes in Health and Disease

(A) IL-4R in GFAP-positive glia.

(B) pSTAT6 and IL-4 in control gels.

(B′) DAPI removed from (B). Asterisks: nuclear pSTAT6.

(C and F) Nuclei of the cells in control (C) and IL-4-treated gels (F) shown in x axis.

(D and G) GFAP and SOX2 in control (D) and IL-4-treated gels (G) shown in x axis.

(E and H) DCX and NEUROD1 in control (E) and IL-4-treated gels (H) shown in x axis.

(I) Quantification of (C–H).

(J–L), GFAP, SOX2, Aβ42 in control (J), Aβ42 (K), and Aβ42 + IL-4 gels (L).

(M–O) DCX, NEUROD1, Aβ42 in control (M), Aβ42 (N), and Aβ42 + IL-4 gels (O). Small panels on the right side of (A)–(F) are single fluorescent channels.

(P) Quantification graphs.

(Q) Pie chart for composition of primary human fetal astrocytes.

(R–R″) Skeletonized connected networks of DCX-positive neurons in (F)–(H).

(S–U) BrdU, GFAP, and Aβ42 in control (L), Aβ42 (M), and Aβ42 + IL-4 gels (N).

(V) Quantification of (J)–(L) for average number of cells normalized to the number of GFAP-positive cells.

(W) Ratio of newborn cells to BrdU-positive GFAP+ cells as an indicator of neurogenic capacity.

(X) Phosphorylated STAT6 immunostaining with DAPI counterstaining for control, Aβ42, and Aβ42 + IL-4 gels.

(Y) Schematics for the consolidated effects of Aβ42 and IL-4 on proliferative plasticity and neurogenic ability in 3D culture model.

Error bars represent the means ± standard deviations. The levels of significance are *p ≤ 0.05, **p ≤ 0.01, and ***p ≤ 0.001. Scale bars, 50 μm (A–H, R–U), 100 μm (J–O), 5 μm (X). All gels: 3 weeks of culture. See also Figures S2, S3, and S6.

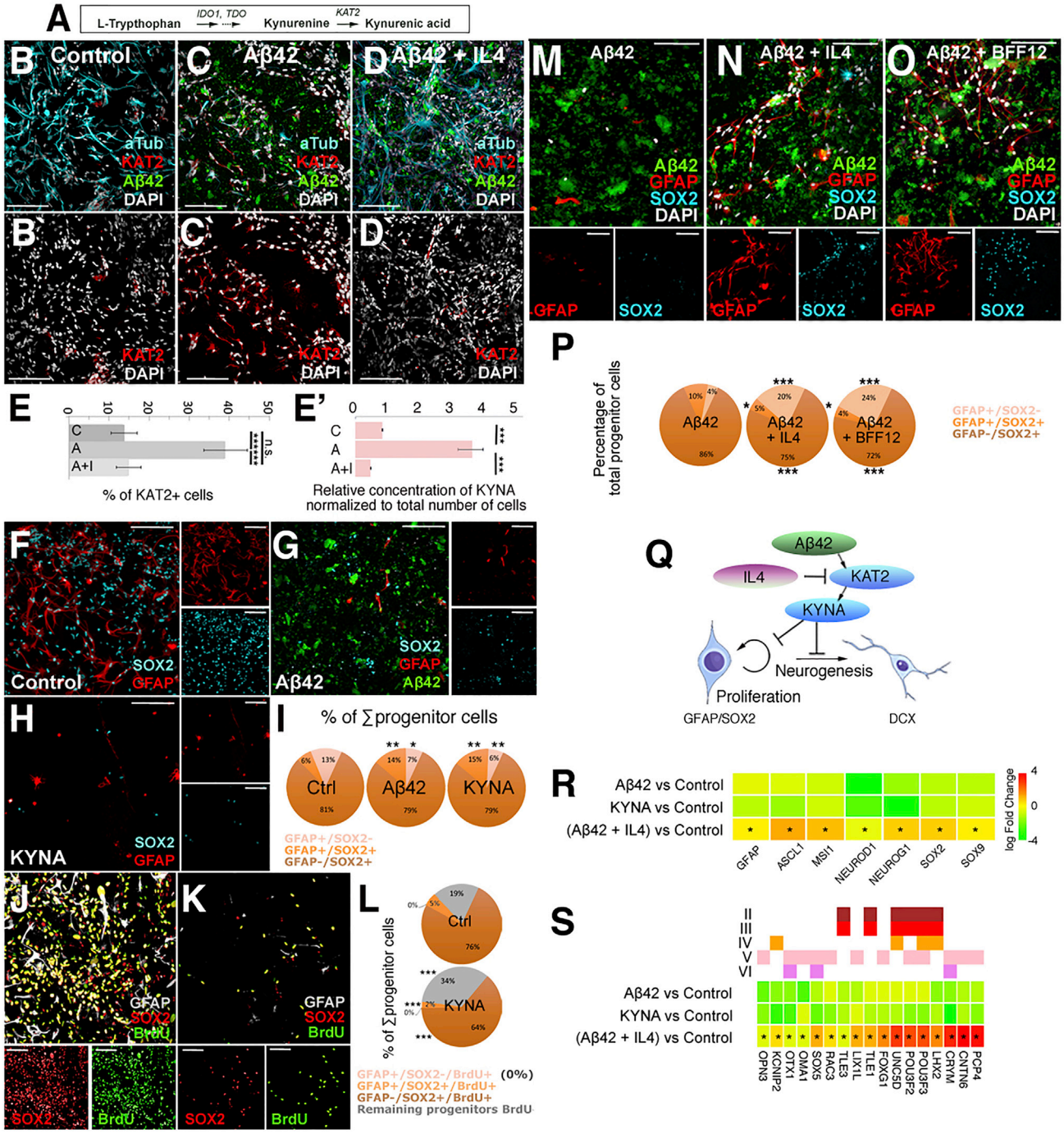

Figure 6. Aβ42 Toxicity Is Mediated by Kynurenic Acid Production by KAT2, and Suppressed by IL-4

(A–D′) Tryptophan metabolism of kynurenic acid. Acetylated tubulin, KAT2, Aβ42 in control (B), Aβ42-treated (C), and Aβ42+IL-treated gels (D). KAT2 is shown alone in (B′)–(D′).

(E) Quantification of abundance of cells expressing KAT2.

(E′) Quantification of KAT2 levels. C, control; A, Aβ42; A + i, Aβ42 + IL-4.

(F–H) SOX2 and GFAP in control (F), Aβ42-treated (G), 10 μM KYNA-treated (H) gels. Single fluorescent channels are on the right.

(I) Composition of GFAP and/or SOX2-expressing cells.

(J and K) GFAP, SOX2, and BrdU in control (J) and KYNA-treated (K) gels.

(L) Composition of proliferating GFAP and/or SOX2-expressing cells.

(M–O) GFAP and SOX2 in Aβ42-treated (M), Aβ42 + IL-4-treated (N), Aβ42 + BFF12-treated gels (O). Lower panels are individual channels.

(P) Composition of GFAP and/or SOX2-expressing cells.

(legend continued on next page)

performing whole transcriptome sequencing, we found that in Aβ42-or KYNA-treated cultures show an overall reduction in NSC marker expression (Figure 6R), while IL-4 treatment with Aβ42 abrogates this reduction and in some cases even enhances the expression levels of progenitor markers (Figure 6R). Since NSC marker expression is restored by IL-4 after Aβ42, we hypothesized that this change in plasticity indicator might be reflected in the replenishment of cortical subtypes. Therefore, we analyzed a set of cortical subtype markers (Figure 6S) and observed that Aβ42 and KYNA treatments reduce the cortical neuronal marker expression in general (Figure 6S), while IL-4 restores or enhances the expression levels of these markers (Figure 6S). These results indicate that IL-4 rescues the neurogenic ability and neuronal network formation after Aβ42 toxicity through restoring the molecular programs that underlie the neurogenic plasticity.

KAT2 is expressed in a subset of astrocytes in the cerebral cortex and hippocampus of rat brains (Guidetti et al., 2007); however, its regulation by AD conditions and Amyloid pathology is unknown. Therefore, to test whether our findings were biologically relevant to AD pathology and could predict the *in vivo* situation, we analyzed the expression of KAT2 in the brains of 12-month-old wild-type and APP/PS1dE9 mouse model of AD (Figures 7A–7D). Compared with cortical and hippocampal regions of controls where KAT2 is detected rather weakly in a few cells (Figures 7A–7A‴ and 7C–7C‴), AD brains strongly increased the KAT2-positive cells (Figures 7B–7B‴, 7D–7D‴, and 7E). In the cortex, non-GFAP+ cells and in the hippocampus the GFAP+ cells seem to be the major source of KAT2 (Figure 7E). Since we found that Amyloid toxicity and KYNA reduces the abundance of SOX2+ cells (Figures 6H and 7A–7D), we asked whether GFAP+ cells would reduce their neurogenic potential in APP/PS1dE9 mouse similar to 3D cultures of pHAs and iPSC-NSCs. Thus, we quantified the percentage of the all GFA + cells that are GFAP+/SOX2+, which is a combination of marker expressions that indicate activated glial cells with neurogenic capacity (Costa et al., 2010; Doetsch, 2003; Heinrich et al., 2010; Laywell et al., 2000; Magnusson and Frisen, 2016; Robel et al., 2011). We found that in AD mice, the percentage of GFAP+/SOX2+ glial cells significantly reduce in cortex (by 54.8%) and hippocampus (by 66.1%) (Figure 7F). These results support our findings that Aβ42 toxicity reduces neurogenic properties of glial cells through upregulation of KAT2 and subsequent production of KYNA.

Since KAT2 is upregulated in AD mouse brains, we hypothesized that if IL-4 has a suppressive role on KAT2 expression, IL-4 must not be activated in AD conditions. We performed immunological staining for IL-4 and GFAP in control and APP/PS1dE9 mouse brains and observed that in the cortex and hippocampus, IL-4 expression was not induced (Figures 7G–7J), suggesting that also *in vivo* IL-4 regulates KAT2 expression. To determine if KAT2 is upregulated in human brains with AD, we performed KAT2 immunostainings on sections of hippocampus and temporal lobe from healthy and AD patients (Figures 7K–7N). We observed that in both the hippocampus and temporal lobe, KAT2-expressing cells elevate in AD brains (Figures 7K–7N), suggesting that KAT2 expression level is a prognostic marker for AD state in human brains and 3D starPEG-heparin-based culture system can be used as a predictive *in vitro* tool for *in vivo* conditions of AD in mammals.

DISCUSSION

Rodent models of AD cannot recapitulate various aspects of human pathology (Gotz and Ittner, 2008; LaFerla and Green, 2012), and in human brains the effects of Aβ42 on NSC plasticity are still controversial (Boekhoorn et al., 2006; Jin et al., 2004; Rodriguez and Verkhratsky, 2011; Waldau and Shetty, 2008). Thus, designing effective stem cell-based regenerative therapies or more targeted drug candidates for the treatment of AD requires assay systems that address the parameters of neurodegenerative pathology individually and in combination in a reductionist humanized setting. We used pHA and iPSC-NSCs to reflect on neurodevelopmental paradigms and neurodegenerative processes. 3D hydrogel cultures using a well-defined star-shaped PEG and heparin that allowed the generation of extensive neuronal networks. Our biohybrid hydrogel system provides valuable advantages by enabling the independent adjustment of biophysical matrix signals, in comparison with chemically undefined matrices where the interpretation of often quite variable results is difficult, and it is rarely possible to dissect the influences of different exogenous and paracrine signals on cellular development in an isolated and controllable experimental setup. Indeed, we determined that starPEG-heparin gels allow faster and more elaborate network formation compared with Matrigel upon identical culture conditions (Figure S1). Compared with previous reports modeling AD in 3D cultures using Matrigel (Choi et al., 2014), despite differences in the initial cell source, starPEG-heparin 3D gels enabled equally elaborate development of neuronal networks, and we believe that these properties of the matrix can offer various advantages, such as high-throughput screening approaches for drug discovery and efficacy tests.

The composition and architecture of the ECM is an integral parameter governing stem cell activity and tissue modeling. However, due to the complex interplay between multiple ECM-derived signals and their pleiotropic effects, *in vivo* assays pose a challenge to identifying the roles of exogenous cues in tissue patterning. Our 3D matrix platform would be advantageous to dissect the roles of matrix properties because cells can dynamically interact with the scaffold to generate their "own" cell-secreted ECM. Additionally, our hydrogels can be covalently functionalized with different matrix-derived peptides or could be used for the effective administration of GAG-affine soluble signal molecules. By doing so, the effects of exogenous cues could be individually tested. Application of customized Aβ42 peptides for

(Q) Schematics for the functional interaction of Aβ42, KAT2, KYNA, and IL-4 in regulating human neural progenitor cell plasticity and neurogenic capacity during AD.

(R) Heatmap for expression changes of neural stem/progenitor cell marker genes in Aβ42, KYNA, and Aβ42 + IL-4 conditions.

(S) Heatmap for expression changes of cortical subtype marker genes in Aβ42, KYNA, and Aβ42 + IL-4 conditions.

Error bars represent the means ± standard deviations. The levels of significance are *$p \leq 0.05$, **$p \leq 0.01$, and ***$p \leq 0.001$. Scale bars, 100 μm. All gels: 3 weeks of culture. See also Figures S2–S6.

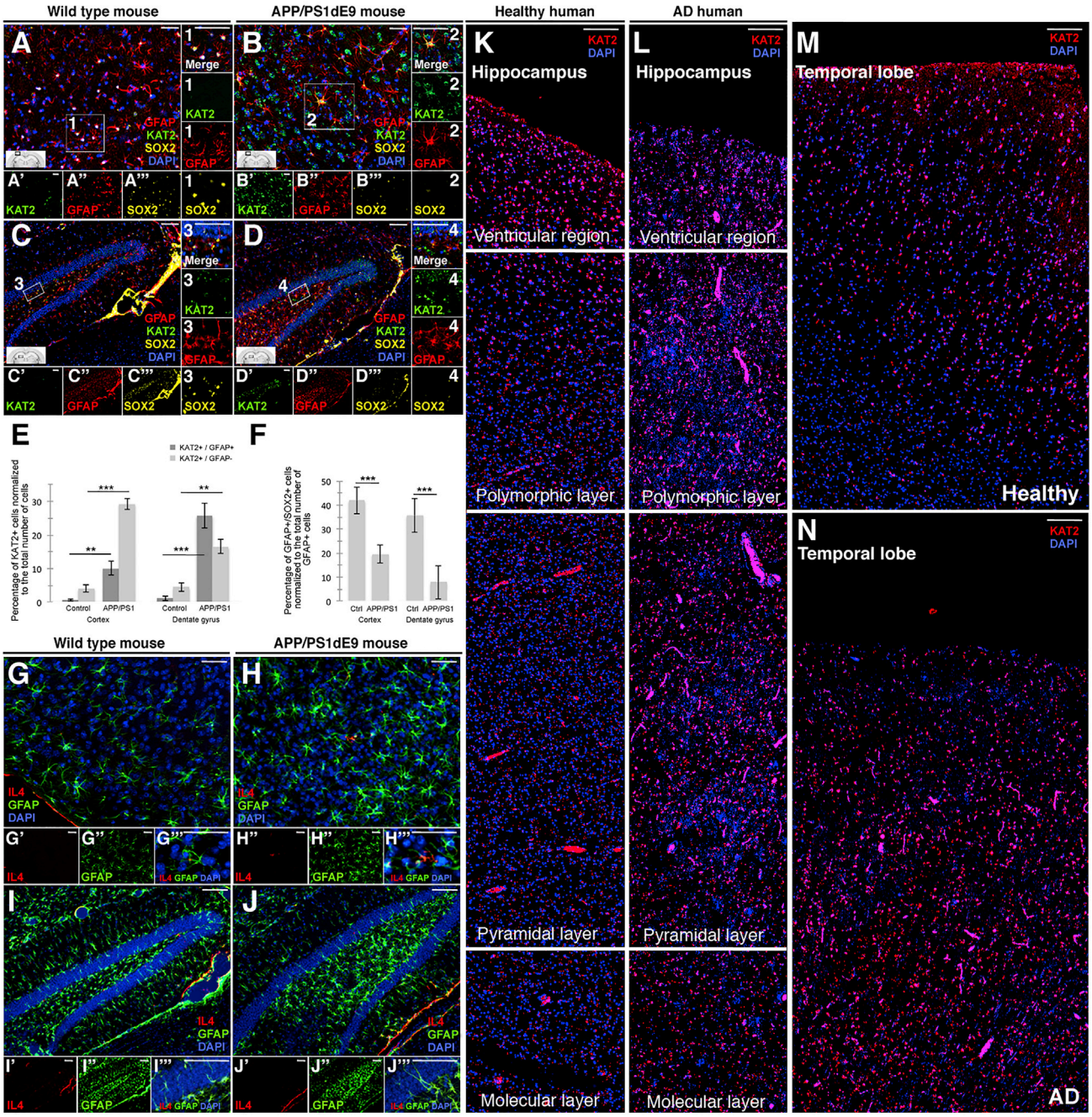

Figure 7. KAT2 Is Upregulated in Mammalian Brains during AD

(A–D‴) GFAP, KAT2, SOX2, and DAPI stainings in wild-type cortex (A), APP/PS1dE9 cortex (B), wild-type hippocampus (C), and APP/PS1dE9 hippocampus (D). Panels with dashed letters under (A)–(D) are single-channel images. Numbered panels (1–4) are enlarged images of the rectangles in main panels (A)–(C).

(E) Quantification graph for the percentage of KAT2+ cells normalized to the total number of cells in wild-type and APP/PS1dE9 cortices and hippocampi.

(F) Quantification graph for the percentage of GFAP+/SOX2+ cells to the total number of GFAP+ cells in wild-type and APP/PS1dE9 cortices and hippocampi.

(G–J) GFAP, IL-4, and DAPI stainings in wild-type cortex (G), APP/PS1dE9 cortex (H), wild-type hippocampus (I), and APP/PS1dE9 hippocampus (J). Panels with dashed letters under (G)–(J) are single-channel images and enlarged merged images.

(K–N) KAT2 and DAPI staining on healthy human hippocampus (K), AD human hippocampus (L), healthy human temporal lobe (M), and AD human temporal lobe (N).

Error bars represent the means ± standard deviations. The levels of significance are *$p \leq 0.05$, **$p \leq 0.01$, and ***$p \leq 0.001$. Scale bars, 50 μm. Mice are 52 weeks old. See STAR Methods text for information on postmortem human tissues.

optimized cellular uptake within the hydrogel-based 3D cultures indicates that the cultures can reciprocate certain aspects of human Aβ42 pathophysiology. Additionally, our gels can be used to experimentally investigate how new cells are incorporated into diseased brains, and how individual differences between cell types and their response to disease stimuli can be measured in a tissue-mimetic composition.

We performed Aβ42 treatment before embedding the cells into the hydrogel. The deliberate reason is the very hypothesis and the question we are postulating on the use of our culture system for assessing the human NSC plasticity during development and disease. Classically, Amyloid toxicity is believed to manifest when there is an existing network and developed glia-neuron structures. However, the linear hypothesis of Aβ42 toxicity on neurons is challenged as Aβ42 affects versatile cell types including the astrocytes that act as NSCs prior to the onset of the classical symptoms. Therefore, NSCs must be neurogenic even in the non-favorable and toxic Amyloid conditions to develop NSC-based therapies. Therefore, we provided NSCs a toxic environment from the very beginning of their journey from proliferation to the neuronal networks. This mode of treatment also allows measuring and assessing the neurogenic response and the network-forming ability of the newborn neurons, which could not be as straightforward as in an already-formed network setting. Thus, we believe that our perspective is suited for designs of stem cell-based restorative/regenerative interventions in AD. Since an important determinant of neurogenic competency of NSCs is neuroinflammatory microenvironment (Kizil et al., 2015b; Kyritsis et al., 2012; Monje et al., 2003; Schwartz et al., 2013), our system can help to address the complex regulation exerted by exogenous factors on neurogenic plasticity of NSCs and survival of neurons in a reductionist assay system simultaneously. We showed that IL-4 has, in addition to its documented neuromodulatory role, a direct effect on pHAs by a previously unknown involvement in KAT2-mediated KYNA production. We would like to note, nevertheless, that our results do not preclude the possibility that additional regulators of KAT2 expression and activity might exist in human brains.

KYNA has a neuroprotective effect (Schwarcz et al., 2012; Stone and Darlington, 2002; Szalardy et al., 2012; Zwilling et al., 2011) but its role in neurogenic progenitors was not known. Here, we demonstrated that KYNA impairs NSC plasticity. This finding is important because the current clinical efforts for enhancing KYNA levels might be effective for neuronal survival but could suppress the neurogenic outcome. These results propose that our 3D culture system can be used to pinpoint previously unidentified roles of neuroinflammatory and metabolic factors during neurodegenerative diseases, and can help to propose a refinement on the clinical practice and drug administration.

IL-4 is an anti-inflammatory factor, and its expression is likely to be contingent upon advanced AD pathology, when Amyloid load and plaques already exist (Heneka et al., 2015; Schwartz et al., 2013). Previously, the beneficial effects of IL-4 on neuronal survival and NSC activity were associated with the reduced inflammatory milieu (Kiyota et al., 2010). However, our system without immune cells indicates that IL-4 establishes a direct crosstalk between the immune system and the neural progenitor compartment, governing plasticity and the neurogenic capacity. Together with elevated KAT2 levels and lack of IL-4 expression in AD model of mice and postmortem AD brain tissues from humans (Figure 7), our findings not only confirm the previous *in vivo* results in zebrafish (Bhattarai et al., 2016) but also provide validation for the use of GAG-based hydrogel culture as an experimentally reliable and reductionist surrogate for predicting *in vivo* circumstances in AD. Therefore, we believe that our 3D cultures can also open up new avenues for tweaking the neuroinflammatory microenvironment toward therapeutically relevant mobilization schemes of endogenous NSCs.

STAR★METHODS

Detailed methods are provided in the online version of this paper and include the following:

- KEY RESOURCES TABLE
- CONTACT FOR REAGENT AND RESOURCE SHARING
- EXPERIMENTAL MODEL AND SUBJECT DETAILS
  - Primary Human Cortical Astrocyte Cultures
  - Induced Pluripotent Stem Cell-Derived Human Neural Stem Cells
  - APP/PS1dE9 Mouse Model of Alzheimer's Disease
  - Post-mortem Human Brain from AD Patients
- METHOD DETAILS
  - Generation of starPEG-Heparin Hydrogels and Cell Encapsulation
  - Generation of Matrigel Cultures
  - Generation of starPEG-Heparin Gels with Induced Pluripotent Stem Cell-Derived Human Neural Stem Cells
  - Synthesis of Amyloid Peptides
  - Aβ42 Treatment
  - Transplantation
  - Immunocytochemistry
  - Western Blots
  - Fluorescent Imaging
  - Histological Analyses
  - Transfection with GCaMP6f Plasmids and Calcium Imaging
  - Patch Clamp Recordings
  - Electron Microscopy
  - Tandem Mass Spectroscopy Coupled to Liquid Chromatography (LC-MS/MS)
  - RNA Isolation
  - Next Generation Sequencing of Whole Transcriptome
- QUANTIFICATION AND STATISTICAL ANALYSIS
  - Image Analysis and Statistics
  - Whole Transcriptome Sequencing Data Analysis
  - Generation of Skeletonized Networks and Quantification
- DATA AND SOFTWARE AVAILABILITY
  - Sequencing Datasets
  - Differential Gene Expression Scripts

SUPPLEMENTAL INFORMATION

Supplemental Information includes six figures, two data files, and seven videos and can be found with this article online at https://doi.org/10.1016/j.devcel.2018.06.005.

ACKNOWLEDGMENTS

This work was supported by DZNE (I2A - Innovation-to-Application Award, C.K.) and Helmholtz Association (VH-NG-1021, C.K.), DFG (KI1524/6, KI1524/10, and KI1524/11, C.K.), (AN797/4–1, C.L.A.) and (CRC-TR67, CRC SFB655, FOR/EXC999, C.W.), and BMBF (PRECIMATRIX-FKZ-03XP0083–310117, C.W.). We wish to thank M. Wagner for electrophysiology, R. Szech for image rendering, and G. Nambirajan and G. Kempermann for APP/PS1dE9 mouse brains.

AUTHOR CONTRIBUTIONS

Conceptualization, C.P. and C.K.; Methodology, C.P. and C.K.; Software, C.P. and M.I.C.; Validation, C.P., H.C., and C.K.; Formal Analysis, C.P., H.C., M.I.C., J.F., W.L., and C.K.; Investigation, C.P., H.C., and C.K.; Resources, C.K., L.B., A.K.T., Y.Z., S.H., C.L.A., U.F., and C.W; Data Curation, C.K.; Funding Acquisition, C.K., C.W., and Y.Z.; Gel Materials, L.B., U.F., and C.W.; Atomic Force Microscopy (AFM) Studies, J.F.; Cell Cultures, C.P., H.C., P.B., K.B., and H.H.; Mouse-Related Work and Stainings on Human Brain Sections, V.M.; RNA Isolation for Deep Sequencing and Subsequent Bioinformatics Analyses, M.I.C.; LC-MS/MS and Amyloid Peptide, W.L. and Y.Z.; Next-Generation Sequencing, M.I.C. and A.D.; Electron Microscopy, T.K.; Patch Clamping and Electrophysiology, X.C., S.H., and C.A.; Writing – Original Draft, C.P., U.F., C.W., and C.K.; Writing – Review & Editing, C.K. and H.C.; Visualization, C.K.; Supervision and Project Administration, C.K.

DECLARATION OF INTERESTS

C.P., U.F., C.W., and C.K. are co-inventors for the patent on the 3D hydrogel system described in this manuscript (PCT/DE2017/100408).

Received: August 25, 2017
Revised: March 6, 2018
Accepted: June 5, 2018
Published: July 2, 2018

REFERENCES

Ahn, S., and Joyner, A.L. (2005). In vivo analysis of quiescent adult neural stem cells responding to Sonic hedgehog. Nature *437*, 894–897.

Alexa, A., Rahnenfuhrer, J., and Lengauer, T. (2006). Improved scoring of functional groups from gene expression data by decorrelating GO graph structure. Bioinformatics *22*, 1600–1607.

Alvarez-Buylla, A., Seri, B., and Doetsch, F. (2002). Identification of neural stem cells in the adult vertebrate brain. Brain Res. Bull. *57*, 751–758.

Arvidsson, A., Collin, T., Kirik, D., Kokaia, Z., and Lindvall, O. (2002). Neuronal replacement from endogenous precursors in the adult brain after stroke. Nat. Med. *8*, 963–970.

Bertram, L., Lill, C.M., and Tanzi, R.E. (2010). The genetics of Alzheimer disease: back to the future. Neuron *68*, 270–281.

Beyreuther, K., and Masters, C.L. (1997). Alzheimer's disease. The ins and outs of amyloid-beta. Nature *389*, 677–678.

Bhattarai, P., Thomas, A.K., Cosacak, M.I., Papadimitriou, C., Mashkaryan, V., Zhang, Y., and Kizil, C. (2017a). Modeling amyloid-β42 toxicity and neurodegeneration in adult zebrafish brain. J. Vis. Exp. *128*, https://doi.org/10.3791/56014.

Bhattarai, P., Thomas, A.K., Papadimitriou, C., Cosacak, M.I., Mashkaryan, V., Froc, C., Kurth, T., Dahl, A., Zhang, Y., and Kizil, C. (2016). IL-4/STAT6 signaling activates neural stem cell proliferation and neurogenesis upon Amyloid-β42 aggregation in adult zebrafish brain. Cell Rep. *17*, 941–948.

Bhattarai, P., Thomas, A.K., Zhang, Y., and Kizil, C. (2017b). The effects of aging on Amyloid-β42-induced neurodegeneration and regeneration in adult zebrafish brain. Neurogenesis (Austin) *4*, e1322666.

Blennow, K., de Leon, M.J., and Zetterberg, H. (2006). Alzheimer's disease. Lancet *368*, 387–403.

Boekhoorn, K., Joels, M., and Lucassen, P.J. (2006). Increased proliferation reflects glial and vascular-associated changes, but not neurogenesis in the presenile Alzheimer hippocampus. Neurobiol. Dis. *24*, 1–14.

Boldrini, M., Fulmore, C.A., Tartt, A.N., Simeon, L.R., Pavlova, I., Poposka, V., Rosoklija, G.B., Stankov, A., Arango, V., Dwork, A.J., et al. (2018). Human hippocampal neurogenesis persists throughout aging. Cell Stem Cell *22*, 589–599.e5.

Bray, L.J., Binner, M., Holzheu, A., Friedrichs, J., Freudenberg, U., Hutmacher, D.W., and Werner, C. (2015). Multi-parametric hydrogels support 3D in vitro bioengineered microenvironment models of tumour angiogenesis. Biomaterials *53*, 609–620.

Chen, T.W., Wardill, T.J., Sun, Y., Pulver, S.R., Renninger, S.L., Baohan, A., Schreiter, E.R., Kerr, R.A., Orger, M.B., Jayaraman, V., et al. (2013). Ultrasensitive fluorescent proteins for imaging neuronal activity. Nature *499*, 295–300.

Choi, S.H., Kim, Y.H., Hebisch, M., Sliwinski, C., Lee, S., D'Avanzo, C., Chen, H., Hooli, B., Asselin, C., Muffat, J., et al. (2014). A three-dimensional human neural cell culture model of Alzheimer's disease. Nature *515*, 274–278.

Cosacak, M.I., Bhattarai, P., Bocova, L., Dzewas, T., Mashkaryan, V., Papadimitriou, C., Brandt, K., Hollak, H., Antos, C.L., and Kizil, C. (2017). Human TAUP301L overexpression results in TAU hyperphosphorylation without neurofibrillary tangles in adult zebrafish brain. Sci. Rep. *7*, 12959.

Cosacak, M.I., Papadimitriou, C., and Kizil, C. (2015). Regeneration, plasticity, and induced molecular programs in adult zebrafish brain. Biomed. Res. Int. *2015*, 769763.

Costa, M.R., Gotz, M., and Berninger, B. (2010). What determines neurogenic competence in glia? Brain Res. Rev. *63*, 47–59.

De Strooper, B., and Karran, E. (2016). The cellular phase of Alzheimer's disease. Cell *164*, 603–615.

Demars, M., Hu, Y.S., Gadadhar, A., and Lazarov, O. (2010). Impaired neurogenesis is an early event in the etiology of familial Alzheimer's disease in transgenic mice. J. Neurosci. Res. *88*, 2103–2117.

Discher, D.E., Mooney, D.J., and Zandstra, P.W. (2009). Growth factors, matrices, and forces combine and control stem cells. Science *324*, 1673–1677.

Doetsch, F. (2003). The glial identity of neural stem cells. Nat. Neurosci. *6*, 1127–1134.

Doetsch, F., Caille, I., Lim, D.A., Garcia-Verdugo, J.M., and Alvarez-Buylla, A. (1999). Subventricular zone astrocytes are neural stem cells in the adult mammalian brain. Cell *97*, 703–716.

Ermini, F.V., Grathwohl, S., Radde, R., Yamaguchi, M., Staufenbiel, M., Palmer, T.D., and Jucker, M. (2008). Neurogenesis and alterations of neural stem cells in mouse models of cerebral amyloidosis. Am. J. Pathol. *172*, 1520–1528.

Fabig, G., Kretschmar, S., Weiche, S., Eberle, D., Ader, M., and Kurth, T. (2012). Labeling of ultrathin resin sections for correlative light and electron microscopy. Methods Cell Biol. *111*, 75–93.

Faiz, M., Sachewsky, N., Gascon, S., Bang, K.W., Morshead, C.M., and Nagy, A. (2015). Adult neural stem cells from the subventricular zone give rise to reactive astrocytes in the cortex after stroke. Cell Stem Cell *17*, 624–634.

Falcon, S., and Gentleman, R. (2007). Using GOstats to test gene lists for GO term association. Bioinformatics *23*, 257–258.

Freudenberg, U., Liang, Y., Kiick, K.L., and Werner, C. (2016). Glycosaminoglycan-based biohybrid hydrogels: a sweet and smart choice for multifunctional biomaterials. Adv. Mater. *28*, 8861–8891.

Gage, F.H., and Temple, S. (2013). Neural stem cells: generating and regenerating the brain. Neuron *80*, 588–601.

Gotz, J., and Ittner, L.M. (2008). Animal models of Alzheimer's disease and frontotemporal dementia. Nat. Rev. Neurosci. *9*, 532–544.

Gregoire, C.A., Goldenstein, B.L., Floriddia, E.M., Barnabe-Heider, F., and Fernandes, K.J. (2015). Endogenous neural stem cell responses to stroke and spinal cord injury. Glia *63*, 1469–1482.

Griffin, W.S.T. (2013). Neuroinflammatory cytokine signaling and Alzheimer's disease. N. Engl. J. Med. *368*, 770–771.

Guidetti, P., Hoffman, G.E., Melendez-Ferro, M., Albuquerque, E.X., and Schwarcz, R. (2007). Astrocytic localization of kynurenine aminotransferase II in the rat brain visualized by immunocytochemistry. Glia *55*, 78–92.

Haass, C., and Selkoe, D.J. (2007). Soluble protein oligomers in neurodegeneration: lessons from the Alzheimer's amyloid beta-peptide. Nat. Rev. Mol. Cell Biol. *8*, 101–112.

Hansen, D.V., Lui, J.H., Parker, P.R., and Kriegstein, A.R. (2010). Neurogenic radial glia in the outer subventricular zone of human neocortex. Nature *464*, 554–561.

Hardy, J., and Selkoe, D.J. (2002). The amyloid hypothesis of Alzheimer's disease: progress and problems on the road to therapeutics. Science *297*, 353–356.

Haughey, N.J., Liu, D., Nath, A., Borchard, A.C., and Mattson, M.P. (2002). Disruption of neurogenesis in the subventricular zone of adult mice, and in human cortical neuronal precursor cells in culture, by amyloid beta-peptide: implications for the pathogenesis of Alzheimer's disease. Neuromolecular Med. *1*, 125–135.

He, N., Jin, W.-L., Lok, K.-H., Wang, Y., Yin, M., and Wang, Z.-J. (2013). Amyloid-β(1-42) oligomer accelerates senescence in adult hippocampal neural stem/progenitor cells via formylpeptide receptor 2. Cell Death Dis. *4*, e924.

Heinrich, C., Blum, R., Gascon, S., Masserdotti, G., Tripathi, P., Sanchez, R., Tiedt, S., Schroeder, T., Gotz, M., and Berninger, B. (2010). Directing astroglia from the cerebral cortex into subtype specific functional neurons. PLoS Biol. *8*, e1000373.

Heneka, M.T., Carson, M.J., El Khoury, J., Landreth, G.E., Brosseron, F., Feinstein, D.L., Jacobs, A.H., Wyss-Coray, T., Vitorica, J., Ransohoff, R.M., et al. (2015). Neuroinflammation in Alzheimer's disease. Lancet Neurol. *14*, 388–405.

Heo, C., Chang, K.-A., Choi, H.S., Kim, H.-S., Kim, S., Liew, H., Kim, J.a., Yu, E., Ma, J., and Suh, Y.-H. (2007). Effects of the monomeric, oligomeric, and fibrillar Aβ42 peptides on the proliferation and differentiation of adult neural stem cells from subventricular zone. J. Neurochem. *102*, 493–500.

Huang, Y., and Mucke, L. (2012). Alzheimer mechanisms and therapeutic strategies. Cell *148*, 1204–1222.

Ittner, L.M., and Gotz, J. (2011). Amyloid-beta and tau–a toxic pas de deux in Alzheimer's disease. Nat. Rev. Neurosci. *12*, 65–72.

Jin, K., Peel, A.L., Mao, X.O., Xie, L., Cottrell, B.A., Henshall, D.C., and Greenberg, D.A. (2004). Increased hippocampal neurogenesis in Alzheimer's disease. Proc. Natl. Acad. Sci. USA *101*, 343–347.

Jones, S.P., Guillemin, G.J., and Brew, B.J. (2013). The kynurenine pathway in stem cell biology. Int. J. Tryptophan Res. *6*, 57–66.

Karow, M., Sanchez, R., Schichor, C., Masserdotti, G., Ortega, F., Heinrich, C., Gascon, S., Khan, M.A., Lie, D.C., Dellavalle, A., et al. (2012). Reprogramming of pericyte-derived cells of the adult human brain into induced neuronal cells. Cell Stem Cell *11*, 471–476.

Kienlen-Campard, P., Miolet, S., Tasiaux, B., and Octave, J.N. (2002). Intracellular amyloid-beta 1-42, but not extracellular soluble amyloid-beta peptides, induces neuronal apoptosis. J. Biol. Chem. *277*, 15666–15670.

Kim, J., Efe, J.A., Zhu, S., Talantova, M., Yuan, X., Wang, S., Lipton, S.A., Zhang, K., and Ding, S. (2011). Direct reprogramming of mouse fibroblasts to neural progenitors. Proc. Natl. Acad. Sci. USA *108*, 7838–7843.

Kim, K., Doi, A., Wen, B., Ng, K., Zhao, R., Cahan, P., Kim, J., Aryee, M.J., Ji, H., Ehrlich, L.I., et al. (2010). Epigenetic memory in induced pluripotent stem cells. Nature *467*, 285–290.

Kiyota, T., Okuyama, S., Swan, R.J., Jacobsen, M.T., Gendelman, H.E., and Ikezu, T. (2010). CNS expression of anti-inflammatory cytokine interleukin-4 attenuates Alzheimer's disease-like pathogenesis in APP+PS1 bigenic mice. FASEB J. *24*, 3093–3102.

Kizil, C., Iltzsche, A., Kuriakose, A., Bhattarai, P., Zhang, Y., and Brand, M. (2015a). Efficient cargo delivery using a short cell-penetrating peptide in vertebrate brains. PLoS One *10*, e0124073.

Kizil, C., Kyritsis, N., and Brand, M. (2015b). Effects of inflammation on stem cells: together they strive? EMBO Rep. *16*, 416–426.

Kriegstein, A., and Alvarez-Buylla, A. (2009). The glial nature of embryonic and adult neural stem cells. Annu. Rev. Neurosci. *32*, 149–184.

Kyritsis, N., Kizil, C., Zocher, S., Kroehne, V., Kaslin, J., Freudenreich, D., Iltzsche, A., and Brand, M. (2012). Acute inflammation initiates the regenerative response in the adult zebrafish brain. Science *338*, 1353–1356.

LaFerla, F.M., and Green, K.N. (2012). Animal models of Alzheimer disease. Cold Spring Harbor Perspect. Med. *2*, https://doi.org/10.1101/cshperspect.a006320.

LaFerla, F.M., Green, K.N., and Oddo, S. (2007). Intracellular amyloid-beta in Alzheimer's disease. Nat. Rev. Neurosci. *8*, 499–509.

Laywell, E.D., Rakic, P., Kukekov, V.G., Holland, E.C., and Steindler, D.A. (2000). Identification of a multipotent astrocytic stem cell in the immature and adult mouse brain. Proc. Natl. Acad. Sci. USA *97*, 13883–13888.

Liao, Y., Smyth, G.K., and Shi, W. (2013). The subread aligner: fast, accurate and scalable read mapping by seed-and-vote. Nucleic Acids Res. *41*, e108.

Liao, Y., Smyth, G.K., and Shi, W. (2014). featureCounts: an efficient general purpose program for assigning sequence reads to genomic features. Bioinformatics *30*, 923–930.

Lilja, A.M., Malmsten, L., Röjdner, J., Voytenko, L., Verkhratsky, A., Ögren, S.O., Nordberg, A., and Marutle, A. (2015). Neural stem cell transplant-induced effect on neurogenesis and cognition in Alzheimer Tg2576 mice is inhibited by concomitant treatment with amyloid-lowering or cholinergic α7 nicotinic receptor drugs. Neural Plast. *2015*, 370432.

Lim, D.A., Huang, Y.C., Swigut, T., Mirick, A.L., Garcia-Verdugo, J.M., Wysocka, J., Ernst, P., and Alvarez-Buylla, A. (2009). Chromatin remodelling factor Mll1 is essential for neurogenesis from postnatal neural stem cells. Nature *458*, 529–533.

Lindvall, O., Kokaia, Z., and Martinez-Serrano, A. (2004). Stem cell therapy for human neurodegenerative disorders—how to make it work. Nat. Med. *10* (*Suppl*), S42–S50.

Love, M.I., Huber, W., and Anders, S. (2014). Moderated estimation of fold change and dispersion for RNA-seq data with DESeq2. Genome Biol. *15*, 550.

Luo, W., and Brouwer, C. (2013). Pathview: an R/Bioconductor package for pathway-based data integration and visualization. Bioinformatics *29*, 1830–1831.

Luzzati, F., Nato, G., Oboti, L., Vigna, E., Rolando, C., Armentano, M., Bonfanti, L., Fasolo, A., and Peretto, P. (2014). Quiescent neuronal progenitors are activated in the juvenile guinea pig lateral striatum and give rise to transient neurons. Development *141*, 4065–4075.

Magnusson, J.P., and Frisen, J. (2016). Stars from the darkest night: unlocking the neurogenic potential of astrocytes in different brain regions. Development *143*, 1075–1086.

Magnusson, J.P., Goritz, C., Tatarishvili, J., Dias, D.O., Smith, E.M., Lindvall, O., Kokaia, Z., and Frisen, J. (2014). A latent neurogenic program in astrocytes regulated by Notch signaling in the mouse. Science *346*, 237–241.

Maitz, M.F., Freudenberg, U., Tsurkan, M.V., Fischer, M., Beyrich, T., and Werner, C. (2013). Bio-responsive polymer hydrogels homeostatically regulate blood coagulation. Nat. Commun. *4*, 2168.

Molyneaux, B.J., Arlotta, P., Menezes, J.R., and Macklis, J.D. (2007). Neuronal subtype specification in the cerebral cortex. Nat. Rev. Neurosci. *8*, 427–437.

Monje, M.L., Toda, H., and Palmer, T.D. (2003). Inflammatory blockade restores adult hippocampal neurogenesis. Science *302*, 1760–1765.

Robel, S., Berninger, B., and Gotz, M. (2011). The stem cell potential of glia: lessons from reactive gliosis. Nat. Rev. Neurosci. *12*, 88–104.

Rodriguez, J.J., and Verkhratsky, A. (2011). Neurogenesis in Alzheimer's disease. J. Anat. *219*, 78–89.

Schirmer, L., Atallah, P., Werner, C., and Freudenberg, U. (2016). StarPEG-heparin hydrogels to protect and sustainably deliver IL-4. Adv. Healthc. Mater. *5*, 3157–3164.

Schwarcz, R., Bruno, J.P., Muchowski, P.J., and Wu, H.Q. (2012). Kynurenines in the mammalian brain: when physiology meets pathology. Nat. Rev. Neurosci. *13*, 465–477.

Schwartz, M., Kipnis, J., Rivest, S., and Prat, A. (2013). How do immune cells support and shape the brain in health, disease, and aging? J. Neurosci. *33*, 17587–17596.

Selkoe, D.J. (2002). Alzheimer's disease is a synaptic failure. Science *298*, 789–791.

Sorrells, S.F., Paredes, M.F., Cebrian-Silla, A., Sandoval, K., Qi, D., Kelley, K.W., James, D., Mayer, S., Chang, J., Auguste, K.I., et al. (2018). Human hippocampal neurogenesis drops sharply in children to undetectable levels in adults. Nature *555*, 377–381.

Stone, T.W., and Darlington, L.G. (2002). Endogenous kynurenines as targets for drug discovery and development. Nat. Rev. Drug Discov. *1*, 609–620.

Sundholm-Peters, N.L., Yang, H.K., Goings, G.E., Walker, A.S., and Szele, F.G. (2005). Subventricular zone neuroblasts emigrate toward cortical lesions. J. Neuropathol. Exp. Neurol. *64*, 1089–1100.

Szalardy, L., Zadori, D., Toldi, J., Fulop, F., Klivenyi, P., and Vecsei, L. (2012). Manipulating kynurenic acid levels in the brain—on the edge between neuroprotection and cognitive dysfunction. Curr. Top. Med. Chem. *12*, 1797–1806.

Taupin, P. (2009). Adult neurogenesis, neural stem cells and Alzheimer's disease: developments, limitations, problems and promises. Curr. Alzheimer Res. *6*, 461–470.

Temple, S. (2001). The development of neural stem cells. Nature *414*, 112–117.

Tincer, G., Mashkaryan, V., Bhattarai, P., and Kizil, C. (2016). Neural stem/progenitor cells in Alzheimer's disease. Yale J. Biol. Med. *89*, 23–35.

Tong, L.M., Fong, H., and Huang, Y. (2015). Stem cell therapy for Alzheimer's disease and related disorders: current status and future perspectives. Exp. Mol. Med. *47*, e151.

Tsurkan, M.V., Chwalek, K., Levental, K.R., Freudenberg, U., and Werner, C. (2011). Modular StarPEG-heparin gels with bifunctional peptide linkers. Macromol. Rapid Commun. *31*, 1529–1533.

Tsurkan, M.V., Chwalek, K., Prokoph, S., Zieris, A., Levental, K.R., Freudenberg, U., and Werner, C. (2013). Defined polymer-peptide conjugates to form cell-instructive starPEG-heparin matrices in situ. Adv. Mater. *25*, 2606–2610.

Venable, J.H., and Coggeshall, R. (1965). A simplified lead citrate stain for use in electron microscopy. J. Cell Biol. *25*, 407–408.

Verpelli, C., Carlessi, L., Bechi, G., Fusar Poli, E., Orellana, D., Heise, C., Franceschetti, S., Mantegazza, R., Mantegazza, M., Delia, D., et al. (2013). Comparative neuronal differentiation of self-renewing neural progenitor cell lines obtained from human induced pluripotent stem cells. Front. Cell. Neurosci. *7*, 175.

Waldau, B., and Shetty, A.K. (2008). Behavior of neural stem cells in the Alzheimer brain. Cell. Mol. Life Sci. *65*, 2372–2384.

Weickenmeier, J., de Rooij, R., Budday, S., Steinmann, P., Ovaert, T.C., and Kuhl, E. (2016). Brain stiffness increases with myelin content. Acta Biomater. *42*, 265–272.

Wieduwild, R., Tsurkan, M., Chwalek, K., Murawala, P., Nowak, M., Freudenberg, U., Neinhuis, C., Werner, C., and Zhang, Y. (2013). Minimal peptide motif for non-covalent peptide-heparin hydrogels. J. Am. Chem. Soc. *135*, 2919–2922.

Wu, T.D., Reeder, J., Lawrence, M., Becker, G., and Brauer, M.J. (2016). GMAP and GSNAP for genomic sequence alignment: enhancements to speed, accuracy, and functionality. Methods Mol. Biol. *1418*, 283–334.

Wyss-Coray, T. (2016). Ageing, neurodegeneration and brain rejuvenation. Nature *539*, 180–186.

Xia, N., Zhang, P., Fang, F., Wang, Z., Rothstein, M., Angulo, B., Chiang, R., Taylor, J., and Reijo Pera, R.A. (2016). Transcriptional comparison of human induced and primary midbrain dopaminergic neurons. Sci. Rep. *6*, 20270.

Young, M.D., Wakefield, M.J., Smyth, G.K., and Oshlack, A. (2010). Gene ontology analysis for RNA-seq: accounting for selection bias. Genome Biol. *11*, R14.

Yu, G., Wang, L.G., Han, Y., and He, Q.Y. (2012). clusterProfiler: an R package for comparing biological themes among gene clusters. OMICS *16*, 284–287.

Zhang, Y., Fussel, S., Reimer, U., Schutkowski, M., and Fischer, G. (2002). Substrate-based design of reversible Pin1 inhibitors. Biochemistry *41*, 11868–11877.

Zwilling, D., Huang, S.Y., Sathyasaikumar, K.V., Notarangelo, F.M., Guidetti, P., Wu, H.Q., Lee, J., Truong, J., Andrews-Zwilling, Y., Hsieh, E.W., et al. (2011). Kynurenine 3-monooxygenase inhibition in blood ameliorates neurodegeneration. Cell *145*, 863–874.

STAR★METHODS

KEY RESOURCES TABLE

REAGENT or RESOURCE	SOURCE	IDENTIFIER
Antibodies		
Anti- IL-4R	Sigma	Cat# SAB4501541; RRID: AB_10745541
Anti-Acetylated tubulin	Sigma	Cat# T6793; RRID: AB_477585
Anti-ASCL1	Neuromics	Cat# MO15048; RRID: AB_2059495
Anti-Aβ42	Cell Signaling Technology	Cat# 8243T
Anti-BrdU	BIO-RAD	Cat# MCA2060; RRID: AB_323427
Anti-CASP3	Santa Cruz Biotechnology	Cat# sc-22140; RRID: AB_2259586
Anti-CRYM	Thermo Fischer	Cat# PA5-65072; RRID: AB_2663317
Anti-CTIP2	Abcam	Cat# ab18465; RRID: AB_2064130
Anti-DBX1	Abcam	Cat# ab156283
Anti-DCX	Invitrogen	Cat# 48-1200; RRID: AB_2533840
Anti-EEA1	Abcam	Cat# ab2900; RRID: AB_2262056
Anti-FOXO1	Thermo Fischer	Cat# MA5-17078; RRID: AB_2538549
Anti-FOXP2	R&D Systems	Cat# AF5647; RRID: AB_2107133
Anti-GFAP	Abcam	Cat# ab7260; RRID: AB_305808
Anti-KAT2	Sigma	Cat# AV43534; RRID: AB_1844405
Anti-MKI67	Abcam	Cat# ab86373; RRID: AB_2142229
Anti-NEUROD1	Abcam	Cat# ab60704; RRID: AB_943491
Anti-Neurofilament (NF-M+H+L)	Life Technologies	Cat# 13-1300; RRID: AB_2532999
Anti-POU3F2	Abcam	Cat# ab94977; RRID: AB_10859580
Anti-PSD95	Thermo Fischer	Cat# MA1-046; RRID: AB_2092361
Anti-RELN	Abcam	Cat# 78540; RRID: AB_1603148
Anti-SATB2	Abcam	Cat# ab51502; RRID: AB_882455
Anti-SOX2	Santa Cruz Biotechnology	Cat# sc-365823; RRID: AB_10842165
Anti-SYN	Millipore	Cat# MAB5258; RRID: AB_2313839
Anti-TUBB3	R&D Systems	Cat# MAB1195; RRID: AB_357520
Anti-VGLUT1	Thermo Fischer	Cat# 48-2400; RRID: AB_2533843
Donkey anti-Goat IgG (H+L), Alexa Fluor 555	Life Technologies	Cat# A-21432; RRID: AB_141788
Donkey anti-Sheep IgG (H+L), Alexa Fluor 555	Life Technologies	Cat# A-21436; RRID: AB_2535857
Goat anti-Mouse IgG (H+L), Alexa Fluor 555	Life Technologies	Cat# A-21422; RRID: AB_141822
Goat anti-Mouse IgG (H+L), Alexa Fluor 647	Life Technologies	Cat# A-21235; RRID: AB_141693
Goat anti-Rabbit IgG (H+L), Alexa Fluor 488	Life Technologies	Cat# A-11008; RRID: AB_143165
Goat anti-Rabbit IgG (H+L), Alexa Fluor 555	Life Technologies	Cat# A-21428; RRID: AB_141784
Goat anti-Rabbit IgG (H+L), Alexa Fluor 647	Life Technologies	Cat# A-21245; RRID: AB_2535813
Goat anti-Rat IgG (H+L), Alexa Fluor 647	Life Technologies	Cat# A-21247; RRID: AB_141778
HRP-coupled secondary antibody	Santa Cruz Biotechnology	Cat# sc-2004; RRID: AB_631746
Biological Samples		
formalin-fixed paraffin-embedded adult human hippocampus section, 54-year old female	BioCat GmbH	Cat# T2234052-BC
formalin-fixed paraffin-embedded Alzheimer's disease adult human hippocampus section, 88-year old male	BioCat GmbH	Cat# T2236052Alz-BC
formalin-fixed paraffin-embedded adult human temporal lobe section, 20-year old male	BioCat GmbH	Cat# T2234078-BC
formalin-fixed paraffin-embedded Alzheimer's disease adult human temporal lobe section, 88-year old male	BioCat GmbH	Cat# T2236078Alz-BC

(*Continued on next page*)

Continued

REAGENT or RESOURCE	SOURCE	IDENTIFIER
Chemicals, Peptides, and Recombinant Proteins		
1-Hydroxybenzotriazole hydrate (HOBT)	Sigma-Aldrich	Cat# 157260
4-Hydroxyquinoline-2-carboxylic acid (Kynurenic acid)	Sigma-Aldrich	Cat# K3375
4–12% Bis-Tris precast gradient gels	NuPage	Cat# NP0322BOX
4',6-diamidino-2-phenylindole (DAPI)	Invitrogen	Cat# D21490
5-Bromo-2′-deoxyuridine (BrdU)	Sigma	Cat# B5002
5-ethynyl-2′-deoxyuridine (EdU)	Invitrogen	Cat# E10415
Acetonitrile (for HPLC)	VWR International	Cat# 83639320
Acetonitrile (for UPLC/LCMS)	Sigma-Aldrich	Cat# 34967-1L
Amyloid-beta42 peptide	Bhattarai et al., 2016	N/A
Astrocyte medium	ScienCell Research Laboratories	Cat# 1801
BFF122	AxonMedChem	Cat# 2237
Dichlormethane (DCM)	MERCK KGaA	Cat# 106050
Diethylether	VWR International	Cat# 23811326
Dimethylformamide	IRIS Biotech GmbH	Cat# SOL-004
Dithiotritol (DTT)	VWR International	Cat# 0281-25G
Fetal Bovine Serum	ScienCell Research Laboratories	Cat# 0010
Fmoc-protected amino acids	IRIS Biotech GmbH	https://www.iris-biotech.de/de/products/amino-acids/the-20-fmoc-standard-aminoacids.html
Formic acid (FA)	MERCK KGaA	Cat# 100264
Geltrex™ LDEV-Free Basement Membrane Matrix	Gibco	Cat# A1413202
GS22™ Neural Supplement 10	Amsbio	Cat# GSM3200
Heparin maleimide conjugate	Tsurkan et al., 2011	N/A
Human FGF-Basic (FGF2, aa1-155)	Gibco	Cat# PHG0261
Human IL-4	Gibco	Cat# PHC0041
L-alanine/L-glutamine	Sigma-Aldrich	Cat# 1012517
Matrigel	BD Biosciences	Cat# 356234
N-Methylmorpholine	Thermo Fischer	Cat# A12158
N,N-Diisopropylethylamine	IRIS Biotech GmbH	Cat# SOL-003
N,N,N′,N′-Tetramethyl-O-(1H- benzotriazol-1-yl)uranium hexafluorophosphate (HBTU)	IRIS Biotech GmbH	Cat# RL-1030
NeuralX™ NSC Medium	Amsbio	Cat# GSM9320
Oxyma	IRIS Biotech GmbH	Cat# RL-1180
penicillin/streptomycin solution	ScienCell Research Laboratories	Cat# 0503
Piperidine	MERCK KGaA	Cat# 822299
PolymerX, bead size 10μm,	Phenomenex Ltd	Cat# 00G-4328-N0
Polytetrafluoroethylene (PTFE)	Sartorius Stedtim	Cat# 11806-50-N
Polyvinylidenefluoride (PVDF)	Carl Roth GmbH + Co.	Cat# KC78.1
Protease inhibitor	Roche	Cat# 4963132001
PVDF membrane	Novex, Life technologies	Cat# LC2002
RGD peptide	Bray et al., 2015	N/A
RIPA Buffer	Sigma	Cat# R0278
Silica particles	Kisker Biotec GmbH	Cat# PSI-10.0
starPEG-MMP-peptide conjugate	Tsurkan et al., 2011	N/A
StemPro™ Accutase™ Cell Dissociation Reagent	Gibco	Cat# A1110501
TentaGel S RAM Fmoc rink amide resin	Rapp Polymere GmbH	Cat# S30023
Thioflavine S	Sigma-Aldrich	Cat# T1892-25G
TO-PRO™-3 Iodide	Thermo Fischer	Cat# T3605

(*Continued on next page*)

Continued

REAGENT or RESOURCE	SOURCE	IDENTIFIER
Trifluoroacetic acid (TFA)	MERCK KGaA	Cat# 808260
Triisopropylsilane (TIS)	MERCK KGaA	Cat# 233781
TurboFectin 8.0	Origene	Cat# TF81001
Western BLoT Ultra Sensitive HRP Substrate	Takara	Cat# T7104A
Experimental Models: Organisms/Strains		
B6C3-Tg(APPswe,PSEN1dE9)85Dbo/Mmjax	The Jackson Laboratory	MMRRC Stock No: 34829-JAX; RRID: MMRRC_034829-JAX
Experimental Models: Cell Lines		
Primary human cortical astrocytes	ScienCell Research Laboratories	Cat# 1800
HIP human neural stem cells	BC1 line, Amsbio	Cat# GSC-4311
Recombinant DNA		
pGP-CMV-GCaMP6f	Chen et al., 2013	www.addgene.org#40755
Software and Algorithms		
clusterProfiler (3.6.0)	Yu et al., 2012	https://bioconductor.org/packages/release/bioc/html/clusterProfiler.html
DESeq2 (1.18.0)	Love et al., 2014	https://bioconductor.org/packages/release/bioc/html/DESeq2.html; RRID: SCR_015687
featureCounts (v1.5.3)	Liao et al., 2013	http://bioinf.wehi.edu.au/featureCounts; RRID:SCR_012919
G-Power	Heinrich Heine Universität Düsseldorf	http://www.gpower.hhu.de/en.html; RRID: SCR_013726
GOSeq (1.30.0)	Young et al., 2010	https://bioconductor.org/packages/release/bioc/html/goseq.html
GOstat (2.44.0)	Falcon and Gentleman, 2007	http://gostat.wehi.edu.au; RRID: SCR_008535
gsnap (version 2016-09-23)	Wu et al., 2016	http://research-pub.gene.com/gmap/; RRID: SCR_005483
KNIME	KNIME AG	https://www.knime.org; RRID: SCR_006164
n-Query	Statistical Solutions Ltd.	https://www.statsols.com/nquery
pathview (1.18.0)	Luo and Brouwer, 2013	https://bioconductor.org/packages/release/bioc/html/pathview.html; RRID: SCR_002732
R scripts for data analyses	This paper	www.kizillab.org/resources
topGO (2.30.0)	Alexa et al., 2006	https://bioconductor.org/packages/release/bioc/html/topGO.html; RRID: SCR_014798
Critical Commercial Assays		
Agencourt® AMPure® Kit	Beckman Coulter	Cat# A63880
NEBNext® Q5 2X PCR Master Mix	New England Biolabs	Cat# M0544
NEBNext® Ultra II Directional RNA Library Prep Kit	New England Biolabs	Cat# E7775S
Total RNA isolation kit	Norgen	Cat# 17200
Deposited Data		
2D primary human astrocyte (control) whole trancriptome sequencing	This paper	GEO: GSE78117
2D primary human astrocyte (Aβ42) whole trancriptome sequencing	This paper	GEO: GSE78117
3D primary human astrocyte (control) whole trancriptome sequencing	This paper	GEO: GSE108038
3D primary human astrocyte (Aβ42) whole trancriptome sequencing	This paper	GEO: GSE108038

(*Continued on next page*)

Continued

REAGENT or RESOURCE	SOURCE	IDENTIFIER
3D induced pluripotent stem cell-derived neural stem cells control whole trancriptome sequencing	This paper	GEO: GSE108038
3D induced pluripotent stem cell-derived neural stem cells (Aβ42) whole trancriptome sequencing	This paper	GEO: GSE108038

CONTACT FOR REAGENT AND RESOURCE SHARING

Further information and requests for resources and reagents should be directed to and will be fulfilled by the Lead Contact, Caghan Kizil (caghan.kizil@dzne.de). A patent on the 3D hydrogel system described in this manuscript is pending (PCT/DE2017/100408). Gel components are available through appropriate MTAs.

EXPERIMENTAL MODEL AND SUBJECT DETAILS

Primary Human Cortical Astrocyte Cultures

Primary human cortical astrocytes (pHAs) isolated from the cerebral cortex of a male fetus at gestation week 21 were obtained from ScienCell Research Laboratory (SRL, Cat. No. 1800) at passage number 1 as frozen stocks. The primary human cortical astrocytes (pHAs) were certified to be negative for HIV-1, HBV, HCV, mycoplasma, bacteria, yeast, and fungi. pHAs were seeded on conventional T75 flasks or 24-well plates and cultured in complete astrocyte medium (AM) composed of Astrocyte medium (SRL, Cat. No. 1801) supplemented with 2% fetal bovine serum (SRL, Cat. No. 0010), 1% astrocyte growth supplement (SRL, Cat. No. 1852) and 1% penicillin/streptomycin solution (SRL, Cat. No. 0503) in an incubator with 5% CO2/95% air atmosphere at 37°C.

Induced Pluripotent Stem Cell-Derived Human Neural Stem Cells

HIP human neural stem cells (iPSC-NSC) (BC1 line, Amsbio, Cat. No. GSC-4311) were obtained commercially. iPSC-NSCs (derived from an adult female) were certified to be negative for HIV-1, HBV, HCV, mycoplasma, bacteria, yeast, and fungi. Cells were seeded in Geltrex™ LDEV-Free Reduced Growth Factor Basement Membrane Matrix (1:200 in complete AM, Gibco, Cat. No. A1413202) precoated culture-ware and maintained in the "expansion medium" composed of NeuralX™ NSC Medium supplemented with 2% GS22™ Neural Supplement 10, 1X Non-Essential Amino Acids, 2mM L-alanine/L-glutamine and 20 ng/ml FGF2. iPSC-NSCs were collected from culture flasks using StemPro™ Accutase™ Cell Dissociation Reagent.

APP/PS1dE9 Mouse Model of Alzheimer's Disease

Brains of B6C3-Tg(APPswe,PSEN1dE9)85Dbo/Mmjax mice were gifts from Govindarajan Nambirajan and Gerd Kempermann. The double transgenic animals were maintained by mating (APP695/0, +/+) females with (+/+, PSEN1/0) males or reciprocal. Littermates of the same sex are kept in the same cage. Animals are kept in the animal husbandry under standard conditions (12 light/12 dark cycle, temperature 23°C with water and pellet food being always accessible). 52 weeks old female mouse brains (control and B6C3-Tg(APPswe,PSEN1dE9)85Dbo/Mmjax) were used for the analyses. Brains were sectioned with vibrotome into 40 μm thick sections, which were then used for immunohistochemical stainings. Four sections were stained from every animal for every experiment (in total 3 mouse brains were used for every staining in Figure 7).

Post-mortem Human Brain from AD Patients

Single formalin-fixed paraffin-embedded 5 micrometer-thick tissue sections were obtained from a commercial source (BioCat GmbH, Germany). Normal adult human hippocampus (T2234052-BC, 54-year old female), Alzheimer's disease adult human hippocampus (T2236052Alz-BC, 88-year old male), normal adult human temporal lobe (T2234078-BC, 20-year old male), Alzheimer's disease adult human temporal lobe (T2236078Alz-BC, 88-year old female) were used. Two sections were stained from every sample.

METHOD DETAILS

Generation of starPEG-Heparin Hydrogels and Cell Encapsulation

StarPEG-heparin hydrogels were generated as previously described (Maitz et al., 2013; Wieduwild et al., 2013) with the following modifications: pHAs at passage 2 were collected from culture flasks using StemPro™ Accutase™ Cell Dissociation Reagent (Gibco, Cat. No. A1110501). After centrifugation (1,200 rpm for 10 minutes), the pHAs were resuspended in PBS at a concentration of 8 x 10^6 cells per ml. For each hydrogel, the cells were first resuspended in 5 μl of PBS, then added 5 μl Heparin maleimide conjugate solution (90 μg/μl in PBS) and 10 μl starPEG-MMP-peptide conjugate solution (Tsurkan et al., 2011) were added to a final volume of 20 μl and a cell density of 2 x 10^6 cells/ml. Next, the 20 μl droplet was placed on a Parafilm sheet for approximately two minutes until it began to gelate. The gels were placed in 24-well plates that contained 1 ml of complete AM per well (Video S7). The gels were cultured and incubated in 5% CO2/95% air at 37°C until the desired time points (1 week, 2 weeks, and 3 weeks). For the Aβ42 treatment

conditions, the cells were incubated with 2 μM Aβ42 for 48 hours prior to harvest and encapsulation to create gels containing Aβ42 pre-treated cells. Then they were mixed with 4 μl of 100 μM Aβ42 peptide diluted in PBS to create a gel environment containing Aβ42. 6 μl of heparin solution (90 μg/μl in PBS) and 10 μl of PEG dissolved in PBS were added to achieve a 1:1 ratio of Heparin maleimide conjugate solution and starPEG-peptide conjugate solution master mix. At this stage, the concentration of Aβ42 was 20 μM, and the concentration of cells in a 20 μl hydrogel was 2 x 10^6 cells/ml. Atomic force microscopy (AFM) was performed (Bray et al., 2015) to determine the mechanical properties of the gels. Briefly, AFM measurements were collected at 37°C using a Nanowizard II AFM (JPK Instruments, Berlin, Germany). Tipless silicon nitride cantilevers with a nominal spring constant of 80 $mN*m^{-1}$ (PNP-TR-TL-Au; Nanoworld) were used. The cantilevers were modified with silica beads (∅10 μm, Kisker Biotec GmbH, Steinfurt, Germany) (Bray et al., 2015). Force-distance curves were acquired in closed loop, constant height mode using a 3 nN contact force and a 5 μm/s approach/retract velocity. Each data set was generated by probing a minimum of 70 different spots on each sample. The data processing software provided by the AFM manufacturer (JPK Instruments) was used to extract the Young's Modulus E from the approach force–distance curves.

Generation of Matrigel Cultures

For the generation of Matrigel cultures, we used BD Matrigel (Cat. No. 356234). Prior to any cell culture work and use of the Matrigel, pipette tips and Eppendorf tubes were frozen at -20°C according to manufacturer's instruction following the ''thick gel method''. The BD Matrigel was thawed overnight on ice at 4°C. pHAs at passage 2 were collected from culture flasks using StemPro™ Accutase™ Cell Dissociation Reagent. After centrifugation (1,200 rpm for 10 minutes), the pHAs were re-suspended in BD Matrigel at 2x10^6 cells per ml. Droplets of the cell/Matrigel mix were placed in the bottom of culture and then placed at 37°C to let them solidify. Then, complete AM (SRL, Catalog Number 1801) was added and the gels cultured for 3 weeks. Cell medium was changed the day after the generation of gels and then every other day.

Generation of starPEG-Heparin Gels with Induced Pluripotent Stem Cell-Derived Human Neural Stem Cells

After centrifugation (1,200 rpm for 10 minutes), the HIP iPSC-NSCs were re-suspended in PBS at a concentration of 8x10^6 cells, and embedded in starPEG-Heparin gels as described before in this manuscript. Apart from the different cell types and the culture medium, the only difference in this procedure of gel preparation was the addition of short RGD peptides as integrin ligands (Bray et al., 2015; Tsurkan et al., 2013). For each hydrogel, the cells were first re-suspended in 5 μl of PBS and then 5 μl of Heparin maleimide conjugate solution (90 μg/μl; Heparin maleimide conjugate solution and 2M of integrin ligands as RGD peptides diluted in PBS via thorough vortexing) and 10 μl of starPEG-peptide conjugate solution were added to a final volume of 20 μl and a final cell density of 2x10^6 cells/ml. Next, the 20 μl droplet was placed on a Parafilm sheet for approximately two minutes until it began to gelate. The gels were placed in 24-well plates that contained 1 ml of expansion medium per well. The gels were cultured and incubated in 5% CO2/95% air at 37°C until the desired time points. The medium we used for pHAs in PEG-Heparin gels gave similar results.

Synthesis of Amyloid Peptides

The peptides were synthesized as previously described (Bhattarai et al., 2016; Kizil et al., 2015a; Wieduwild et al., 2013). For peptide synthesis, all of the required chemicals were purchased from IRIS Biotech GmbH (Marktredwitz, Germany). Acetonitrile (for UPLC/LCMS), dichloromethane (DCM), diethylether, dimethyl sulfoxide (DMSO), formic acid (FA), trifluoroacetic acid (TFA), and triisopropylsilane (TIS) were purchased from MERCK KGaA (Darmstadt, Germany). Acetic anhydride and N-methylmorpholine (NMM) were purchased from Sigma-Aldrich Co. LLC (St. Louis, MO, USA). Dithiothreitol (DTT) was obtained from Prolab VWR International, LCC (Radnor, PA, USA). Acetonitrile (for HPLC) was purchased from TH Geyer (Renningen, Germany). 5(6)-Carboxyfluorescein was purchased from Acros Organics (Fisher Scientific Company LLC). The TentaGel S RAM Fmoc rink amide resin was purchased from RappPolymere GmbH (Tübingen, Germany). The peptide synthesis columns and syringes with included filters were purchased from Intavis AG (Cologne, Germany). Water was obtained from a Milli-Q water purifier (Milli-Q Advantage A10, EMD Millipore Corporation, Billerica, MA, USA) with a LCPAK0001 Milli-Q filter. The polytetrafluoroethylene (PTFE) filter, polyvinylidene fluoride (PVDF) syringe filter, and filter holder were purchased from Sartorius Stedtim (Aubagne, France).

Aβ42 peptides were prepared using standard 9-fluorenylmethoxycarbonyl (Fmoc) chemistry with 2-(1H-benzotriazol-1-yl)-1,1,3,3-tetramethyluronoium hexafluorophosphate (HBTU) activation on an automated solid-phase peptide synthesizer (ResPep SL, Intavis) (Wieduwild et al., 2013; Zhang et al., 2002). Each amino acid was coupled twice at 5-fold excess followed by capping the non-reacted amino groups with acetic anhydride to achieve high quality synthesis. Upon completion of the peptide synthesis, 5(6)-carboxyfluorescein was coupled to the N-terminus using HBTU as the coupling reagent. The peptide was then cleaved from the resin with TFA/TIS/water/DTT (90(v/v):5(v/v):2.5(v/v):2.5(m/v)) for 2 hours. The product was precipitated and washed with ice-cold diethyl ether.

The peptide was dissolved in Milli-Q water, and peptide purification was performed via reverse-phase high-pressure liquid chromatography (HPLC) on a semi-preparative HPLC (Waters) equipped with a semi-preparative column (PolymerX RP-1, 250 x 10 mm, Phenomenex). The peptide was eluted from the column by applying a gradient of 5% to 100% solvent B over 30 min at 20 ml/min, in which solvent A is 0.1% TFA in water and solvent B is 0.1% TFA and 5% water in acetonitrile.

Purity was confirmed on an analytical reverse phase ultra-high pressure liquid chromatograph (UPLC Aquity with UV Detector) equipped with an analytical C18 column (Acquity UPLC BEH C18, bead size 1.7 μm, 50 x 2.1 mm) using an isocratic gradient and electrospray ionization mass spectrometry (ESI-MS) (Acquity TQ Detector).

Aβ42 Treatment

The Aβ42 treatment was performed 24 hours post-thaw for a period of 48 hours at 10 μM final concentration for 3D pHA and 3D iPSC-NSC cultures. Amyloid plaques remain in the culture attached to the cells throughout the cultures. The medium was removed and the cells were washed with PBS after 48 h Aβ42 treatment. Then, the cells were collected using Accutase, counted and centrifuged at 271 g for 10 min. The cell pellet was resuspended in PBS to obtain at 8.10^6 cells/ml. This cell suspension was mixed with an equal volume of 6 mM heparin maleimide conjugate in PBS to obtain a 3.00 mM heparin maleimide conjugate-cell suspension mix at 4.10^6 cells/ml. 10 μl of this mix was combined with 10 μl of 2.25 mM starPEG-MMP-peptide conjugate solution in PBS (Tsurkan et al., 2011), quickly triturated a few times, and the resulting 20 μl volume was pipetted onto a Parafilm sheet forming a droplet. This droplet was allowed to gelate for about 2 min resulting in formation of a 20 μl hydrogel containing 40,000 cells (2.0 x 106 cells/ml) at a final concentration of 1.5 mM heparin maleimide conjugate and 1.12 mM starPEG-MMP-peptide conjugate. The gels were then placed in 0.75 ml of AM culture medium per well in 24-well plates, and incubated in 5% CO2/95% air at 37°C until the desired time points (1 week, 2 weeks, and 3 weeks). The medium was changed 3 times a week throughout the incubation period.

2D pHA cultures were treated with 2 μM Aβ42 in the culture medium for 48 hours between second and fourth days of culture. The medium is removed and cells are washed with cell culture medium twice. Amyloid plaques remain in the culture attached to the cells throughout the cultures. New medium is added and cultures were continued.

Transplantation

Primary human fetal cortical astrocytes (pHAs) were cultured for two days and treated with TO-PRO™-3 Iodide (Thermo Scientific, Cat. No. T3605) for 1 hour before transplantation. After a washing step, the cells were harvested with StemPro™ Accutase™ Cell Dissociation Reagent and re-suspended in complete AM at $3x10^5$ cells per ml. With a pipette tip, 2 μl of the cell suspension was injected into the center of the hydrogel. After a week of culture, the hydrogels were fixed and processed for immunocytochemistry.

Immunocytochemistry

All of the hydrogels were fixed with ice-cold 4% paraformaldehyde and incubated for 1.5 hours at room temperature followed by washing in PBS overnight at 4°C. For immunocytochemistry, the hydrogels were blocked and permeabilized in blocking solution for 4 hours at room temperature. For BrdU- treatment, the gels were incubated with 2 M HCl for 20 minutes at 37°C followed by three washes in PBS (2 hours each). EdU staining was performed according to the manufacturer's protocol (Life Technologies, Cat. No. C10638). Briefly, after fixation with 4% PFA, gels were incubated in Click-iT® fixative (Life Technologies, Cat. No. C10418) and 1X Click-iT® EdU buffer was applied. Click-iT® EdU Reaction Cocktail was prepared by adding 20 μl of CuSO4 to 100 μl of the reaction buffer, 875 μl PBS and 5 μl of Alexa Fluor® 488 azide (Thermo Scientific, Cat. No. C10425), and the reaction was developed for 1 hour. The hydrogels were incubated with primary antibodies in blocking solution overnight at 4°C. The gels were washed for two subsequent days at 4°C, with occasional changes of the PBS. After washing, the gels were incubated with the secondary antibodies (1:500 in blocking solution) at room temperature for 6 hours. After 3 washing steps of 2 hours each, DAPI staining was performed (1:3000 in PBS, 2 hours at room temperature, Invitrogen, Cat. No. D21490). Immunostaining for SOX2 (1:100, Santa Cruz Biotechnology, Cat. No. sc-365823, sc-17319), SATB2 (1:300, Abcam, Cat. No. ab51502), ASCL1 (1:100, Neuromics, Cat. No. MO15048), CTIP2 (1:100, Abcam, Cat. No. ab18465), EEA1 (1:500, Abcam, Cat. No. ab2900), neurofilament (NF-M+H+L) (1:500, Life Technologies, Cat. No. 13-1300), TUBB3 (1:500, R&D Systems, Cat. No. MAB1195), CASP3 (1:500, Santa Cruz Biotechnology, Cat. No. sc-22140), MKI67 (1:1000, Abcam, Cat. No. ab86373), acetylated tubulin (1:500, Sigma, Cat. No. T6793), SYN (1:500, Millipore, Cat. No. MAB5258), GFAP (1:500, Abcam, Cat. No. ab7260), DCX (1:300, Invitrogen, Cat. No. 48-1200), Aβ42 (1:500, Cell Signaling Technology, Cat No. 8243), Reelin (1:500, Abcam, Cat. No. ab78540), FOXO1 (1:100, Thermo Fisher Scientific, Cat. No. MA5-17078), FOXP2 (1:10, R&D, Cat. No. AF5647), POU3F2 (1:100, Abcam, Cat. No. ab94977). CRYM (1:25, Thermo Fisher Scientific, Cat. No. PA5-65072), NEUROD1 (1:500, Abcam, Cat. No. ab60704), PSD95 (1:300, Thermo Fischer, Cat. No. MA1-046), DBX1 (1:300, Abcam, Cat. No. ab156283), VGLUT1 (1:500, Thermo Fischer, Cat. No. 48-2400), BrdU (1:500, BIO-RAD, Cat. No. MCA2060), KAT2 (1:300, Sigma, Cat. No. AV43534), and IL-4R (1:250, Sigma, Cat. No. SAB4501541) were performed. All of the secondary antibodies were purchased from Life Technologies: Goat anti-Mouse IgG (H+L) Cross-Adsorbed Secondary Antibody, Alexa Fluor 555, Cat. No. A-21422; Goat anti-Rabbit IgG (H+L) Cross-Adsorbed Secondary Antibody, Alexa Fluor 488, Cat. No. A11008; Goat anti-Rat IgG (H+L) Cross-Adsorbed Secondary Antibody, Alexa Fluor 647, Cat. No. A-21247; Donkey anti-Sheep IgG (H+L) Cross-Adsorbed Secondary Antibody, Alexa Fluor 555; A-21436; Donkey anti-Goat IgG (H+L) Cross-Adsorbed Secondary Antibody, Alexa Fluor 555, Cat. No. A-21432; Goat anti-Rabbit IgG (H+L) Cross-Adsorbed Secondary Antibody, Alexa Fluor 555, Cat. No. A-21428; Goat anti-Rabbit IgG (H+L) Highly Cross-Adsorbed Secondary Antibody, Alexa Fluor 647, Cat. No. A-21245; Goat anti-Mouse IgG (H+L) Cross-Adsorbed Secondary Antibody, Alexa Fluor 647, A-21235).

Western Blots

For western blotting, gels were mechanically disrupted and total protein was isolated using as described (Cosacak et al., 2017) and as follows: 200 μL RIPA buffer (Sigma, R0278) was used with addition of protease inhibitors (Roche, Catalog number 04963132001). 5 μl of protein ladder (ThermoFisher, #26634) and 10 μl of total protein was loaded in 4–12% Bis-Tris precast gradient gels (NuPage, Catalog number NP0322BOX) and the gels were run in NuPAGE MES SDS running buffer (Novex, Life technologies, NP0006-1) at 200 V for 60 min. Blots were transferred to methanol activated PVDF (Novex, Life technologies, LC2002) membrane, and were blocked in 10% milk powder in 0.2% Tween in 1X-PBS for 1 hour at room temperature. The primary antibodies at appropriate

dilutions in 2 ml 0.2% Tween in 1X-PBS were applied overnight at 4°C in 15 or 50 ml plastic containers. Following the washing steps, secondary antibodies at 1:4000 dilutions (HRP-coupled, Santa Cruz, #sc-2004) were applied at room temperature for 2 hours. Gel images were acquired by ImageQuant LAS4000 (GE Healthcare) using Western BLoT Ultra Sensitive HRP Substrate (Takara, #T7104A). Band intensities were calculated using ImageJ.

Fluorescent Imaging

For the hydrogels, fluorescent imaging was performed using a Leica SP5 inverted Laser Scanning Confocal microscope. The hydrogels were placed in glass bottom Petri dishes. Sixty microliters of PBS were added on top of the hydrogels to avoid desiccation. The Z-stacks were captured using a 25x water immersion lens. Every Z-stack had a z-distance of 500 μm. Monolayers were imaged using an inverted Zeiss Apotome 2 microscope.

Histological Analyses

For Gallyas silver staining, the 3D hydrogels were cryo-frozen and sequentially incubated in 5% periodic acid (5 minutes), an alkaline silver iodide solution (1 minute), acetic acid (3 minutes), 0.1% gold chloride (5 minutes), 1% sodium thiosulfate (5 minutes), and 2.5% aluminum sulfate (1 minutes), with intermittent washes with distilled water. For Thioflavin S staining, samples were incubated in 1% Thioflavin S (8 minutes), absolute ethanol (3 minutes), and DAPI (10 minutes).

Transfection with GCaMP6f Plasmids and Calcium Imaging

TurboFectin 8.0 reagent (OriGene, Cat# TF81001) was used to transfect adherent (2D cultures) and encapsulated (3D cultures) cells with 700 μg plasmid per reaction in 1 ml of cell growth medium. The pGP-CMV-GCaMP6f plasmid was a gift from Douglas Kim (Addgene plasmid # 40755) (Chen et al., 2013). The images were captured using a Leica SP5 inverted Laser Scanning Confocal microscope in resonant scanner mode with photon counting. Images were acquired every 100 milliseconds. Analysis of the calcium image spectrum was performed with the Leica LAS AF software by using region of interests (ROIs) and photon counting.

Patch Clamp Recordings

Single neurons were recorded in Artificial Cerebrospinal Fluid (ACSF) (119 mM NaCl, 2.5 mM KCl, 2 mM $CaCl_2$, 1.3 mM $MgCl_2$, 1 mM NaH_2PO_4, and 10 mM glucose, pH 7.3) and patched with nerve solution (125 mM K^+-gluconate, 0.1 mM $CaCl_2$, 0.6 mM $MgCl_2$, 8 mM NaCl, 1 mM EGTA, 0.01 mM HEPES, and 4 mM Na-ATP, pH 7.23) The Whole-cell patch recordings were assessed using a HEKA set up and Pulse program. Membrane voltage resistance was held at -80 mV with the pipette resistance of 4-6 MOhms. For measurements of K+ and Na+ currents, test pulses were applied in 80 ms durations from -80 mV to 30 mV every 2 s. All experiments were done at 20-23°C.

Electron Microscopy

For electron microscopy, the hydrogel-embedded cells were fixed in modified Karnovsky's fixative (2% glutaraldehyde + 2% paraformaldehyde in 50 mM HEPES) at least overnight at 4°C. The samples were washed 2x in 100 mM HEPES and 2x in water and post-fixed in a 2% aqueous OsO_4 solution containing 1.5% potassium ferrocyanide and 2 mM $CaCl_2$ for 30 min on ice. Next, washes in water, 1% thiocarbohydrazide in water (20 minutes at room temperature), water, and a second osmium contrasting step in 2% OsO_4/water (30 minutes on ice). After several washes in water, the samples were *en bloc* contrasted with 1% uranyl acetate/water for 2 hours on ice, washed again in water, dehydrated in a graded series of ethanol/water up to 100% ethanol, and infiltrated with Epon 812 (Epon/ethanol mixtures: 1:3, 1:1, 3:1 for 1.5 hours each, pure Epon overnight, and pure Epon for 5 hours). The samples were embedded in flat embedding molds and cured overnight at 65°C. Ultrathin sections were prepared with a Leica UC6 ultramicrotome (Leica Microsystems, Vienna, Austria), collected on Formvar-coated slot grids and stained with lead citrate and uranyl acetate (Venable and Coggeshall, 1965).

For CLEM, cells that were embedded in the hydrogels with the fluorescein-labeled peptide were fixed with 4% paraformaldehyde in 100 mM phosphate buffer (PB). After several washes in water, the samples were dehydrated in 50% (15 minutes at 4°C), 70%, 90%, and 100% acetone (45 minutes each at -25°C) and incubated with LR Gold (London Resin Company, Reading, UK) solutions of 33% and 66% LR Gold/acetone, pure LR Gold (1 hour each at -25°C), and LR Gold + 0.1% benzil (1 hour, overnight at -25°C). Finally, the samples were transferred to LR Gold-containing 1% benzil and polymerized using the UV lamp of the Leica AFS2 freeze substitution unit (Leica Microsystems, Vienna, Austria) for 48 hours at -25°C. Ultrathin sections were mounted on Formvar-coated EM grids, stained with DAPI, imaged with a wide field fluorescence microscope, washed, and contrasted with 1% uranyl acetate for EM (Fabig et al., 2012). Contrasted ultrathin sections were analyzed on a FEI Morgagni D268 (FEI, Eindhoven, The Netherlands) or a Jeol JEM1400 Plus at 80 kV acceleration voltage.

Tandem Mass Spectroscopy Coupled to Liquid Chromatography (LC-MS/MS)

For LC-MS/MS, the culture media in last week (Day 15-21) were collected during the medium change for untreated (control), Aβ42-treated, IL-4-treated, and Aβ42+IL-4-treated gels. In total, 10 ml of medium for every condition from 6 gels per experimental group was collected. The quantification of Kynurenic acid (KYNA) was performed by tandem mass spectrometry (MS/MS) coupled to liquid chromatography (LC-MS/MS) using waters ACQUITY UPLC system with ACQUITY TQ Detector. The UPLC was equipped with an analytical C18 column (ACQUITY UPLC ® BEH C18 1.7 μm, 2.1 × 50 mm). The samples with 10 μL of the volume were injected to the column. To avoid the contamination between the samples, 3 injections of PBS was performed after each sample measurement.

Water with 0.1% formic acid was used as solvent A and acetonitrile with 0.1% formic acid as solvent B. The time curve for running: 0.0-1.0 min, 100% buffer A; 1.0-4.0 min, a linear gradient running from 100% buffer A to 100% buffer B; 4.0 min to 5.0 min, 100% buffer B; 5.0 min to 5.5 min, a linear gradient running from 100% buffer B to 100% buffer A; 5.5 min to 6.0 min, 100% buffer A. For MS/MS analysis of KYNA, the TQ detector was set in multiple reaction monitoring (MRM) to detect the parent (189.95 m/z) and the daughter (88.98 m/z), with 2770V of the capillary voltage, 32V of the cone energy, 40V of the collision energy and 0.328s of the dwell time.

RNA Isolation

RNA isolation from 2D cell culture was performed by Trizol (Invitrogen). Total RNA isolation from 3D gels was performed by Norgen Total RNA isolation Kit (Cat# 17200). 5 gels were lysed in 1 ml RL buffer with 10 μL β-mercaptoethanol, and after centrifugation at 12,000 g for 7 min at room temperature, the supernatant was collected in a new Eppendorf and mixed with absolute Ethanol (Bhattarai et al., 2016).

Next Generation Sequencing of Whole Transcriptome

cDNA libraries were prepared by following the protocol for NEBNext® Ultra I Directional RNA Library Prep Kit. This involves the following steps: mRNA isolation via poly(A)+ selection and fragmentation, first strand and second strand cDNA synthesis, purification using the Agencourt® AMPure® Kit and end repair/dA-tailing of cDNA. Adapters were ligated to the dA-tailed cDNA, followed by an size selection using AMPure XP Beads. Indexing of the library constructs was done with illumina® index primer during the following PCR amplification using NEBNext® Q5 2X PCR Master Mix. Lastly, libraries were purified using the Agencourt® AMPure® Kit. Libraries were pooled and sequenced on an illumina® NextSeq 500 system, resulting in ca. 27 – 38 million 75 bp single-end reads. All protocols are performed according to the manufacturers' instructions.

QUANTIFICATION AND STATISTICAL ANALYSIS

Image Analysis and Statistics

The 3D reconstructions of hydrogel images and videos were generated using Arivis 4D software. Images from histological sections were acquired using Zeiss ZEN software. Counting was performed on acquired images. The statistical analyses were performed using GraphPad Prism and two-tailed Student's t-tests. The levels of significance were *: $p \leq 0.05$, **: $p \leq 0.01$, and ***: $p \leq 0.001$. In all graphs, means ± standard deviations are shown in figures and figure legends.

The effect size was calculated using G-Power, and the sample size was estimated with n-Query. The data conforms to normal distribution as determined by Pearson's chi-squared test. The variations between the samples are similar as determined by variance estimation using Microsoft Excel software. For 3D gels, 9 gels were used for quantifications (3 technical replicates in every experiment, and 3 experiments as biological replicates). All experiments were replicated many times in the laboratory and results were confirmed independently (80-120 gels were qualitatively analyzed to check the consistency of the results for every individual experiment). All samples were included in the analyses.

Whole Transcriptome Sequencing Data Analysis

The reads in fastq files were aligned to the human genome (hg19/GRCh38) with gsnap (version 2016-09-23) (Wu et al., 2016), and featureCounts (v1.5.3) (Liao et al., 2013, 2014) was used to assign reads to each gene using Ensembl version 90 [Homo_sapiens.GRCh38.90.gtf]. DESeq2 (1.18.0) (Love et al., 2014) was used to normalize the reads, calculate fold changes and p-values. 2-fold change and padj value of less than 0.1 were used to identify differentially expressed genes. For KEGG pathway analysis GOstats (2.44.0) (Falcon and Gentleman, 2007), GOSeq (1.30.0) (Young et al., 2010), and clusterProfiler (3.6.0) (Yu et al., 2012) were used. topGO (2.30.0) (Alexa et al., 2006) was used for GO analysis and pathview (1.18.0) (Luo and Brouwer, 2013) was used for drawing KEGG pathway. Results are shown in Data S1 and S2.

Generation of Skeletonized Networks and Quantification

To examine the axons of neural cells, the length and branching were obtained by thinning binary images to a skeleton, which was performed in all three dimensions. In detail, the raw images were processed with a Gaussian filter and then with the tubeness filter to enhance linear structures. Then, an automatic threshold was applied, followed by several morphological operations to facilitate the skeletonization. Fiji software (www.fiji.sc) was used for image processing. Skeletons were quantified using KNIME freeware.

DATA AND SOFTWARE AVAILABILITY

Sequencing Datasets

All deep sequencing experiments (2D pHA, 3D pHA, 3D iPSC-NSC control and Aβ42-treated) have been deposited in the GEO database (https://www.ncbi.nlm.nih.gov/geo/) under the ID codes GEO: GSE78117 and GEO: GSE108038.

Differential Gene Expression Scripts

All data analysis pipeline scripts were written using R package in our laboratory and can be found under www.kizillab.org/resources.

Developmental Cell, Volume *46*

Supplemental Information

3D Culture Method for Alzheimer's Disease Modeling Reveals Interleukin-4 Rescues Aβ42-Induced Loss of Human Neural Stem Cell Plasticity

Christos Papadimitriou, Hilal Celikkaya, Mehmet I. Cosacak, Violeta Mashkaryan, Laura Bray, Prabesh Bhattarai, Kerstin Brandt, Heike Hollak, Xin Chen, Shuijin He, Christopher L. Antos, Weilin Lin, Alvin Kuriakose Thomas, Andreas Dahl, Thomas Kurth, Jens Friedrichs, Yixin Zhang, Uwe Freudenberg, Carsten Werner, and Caghan Kizil

Supplementary Information

Supplementary figures and legends

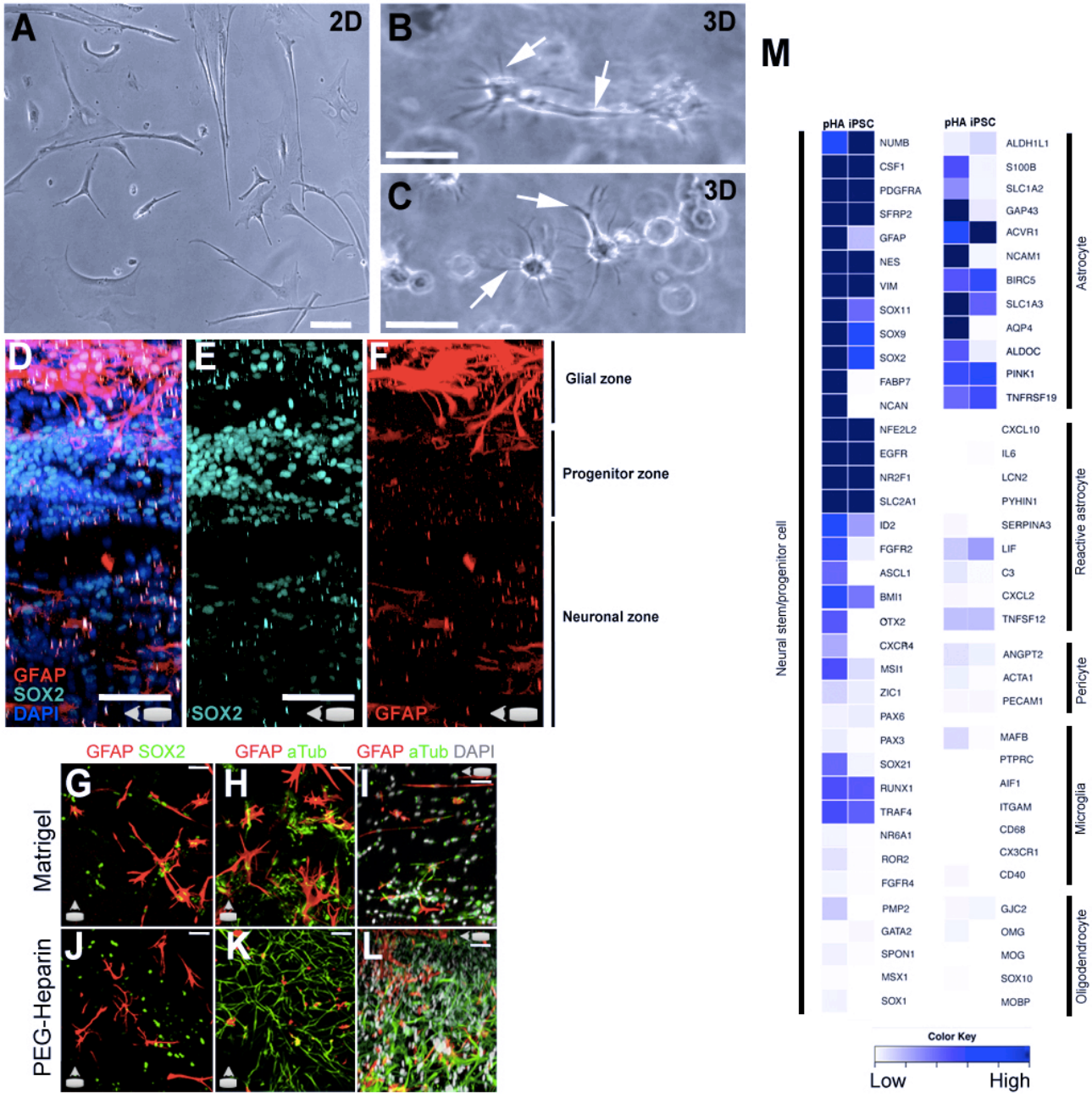

Figure S1, related to Figure 1
3D topology of neuronal networks and progenitor zones in starPEG-Heparin hydrogels and comparison to Matrigel cultures

(A) Culture of primary human fetal cortical astrocytes (pHA) in 2D.
(B,C) Culture of pHAs in 3D. Note the arborized morphology and cellular processes reminiscent of in vivo (white arrows).
(D) GFAP and SOX2 immunostaining with DAPI counterstain in X-view of a 3D culture.
(E) SOX2 channel from D.
(F) GFAP channel from D.
(G) Immunostaining for GFAP and SOX2 in Matrigel cultures.
(H) Immunostaining GFAP and Acetylated tubulin in Matrigel cultures Z-view.
(I) Immunostaining GFAP and Acetylated tubulin in Matrigel cultures X-view.
(J) Immunostaining for GFAP and SOX2 in starPEG-Heparin cultures.
(K) Immunostaining GFAP and Acetylated tubulin in starPEG-Heparin cultures Z-view.
(L) Immunostaining GFAP and Acetylated tubulin in starPEG-Heparin cultures X-view.
(M) Heat map of expression levels of various cell type markers for neural stem cells, astrocytes, reactive astrocytes, pericytes, microglia and oligodendrocytes in pHA and iNSC cultures.
Scale bars 25 μm in A-C, 100 μm in D-F, and 20 μm in G-L. All gels are 3 weeks of culture.

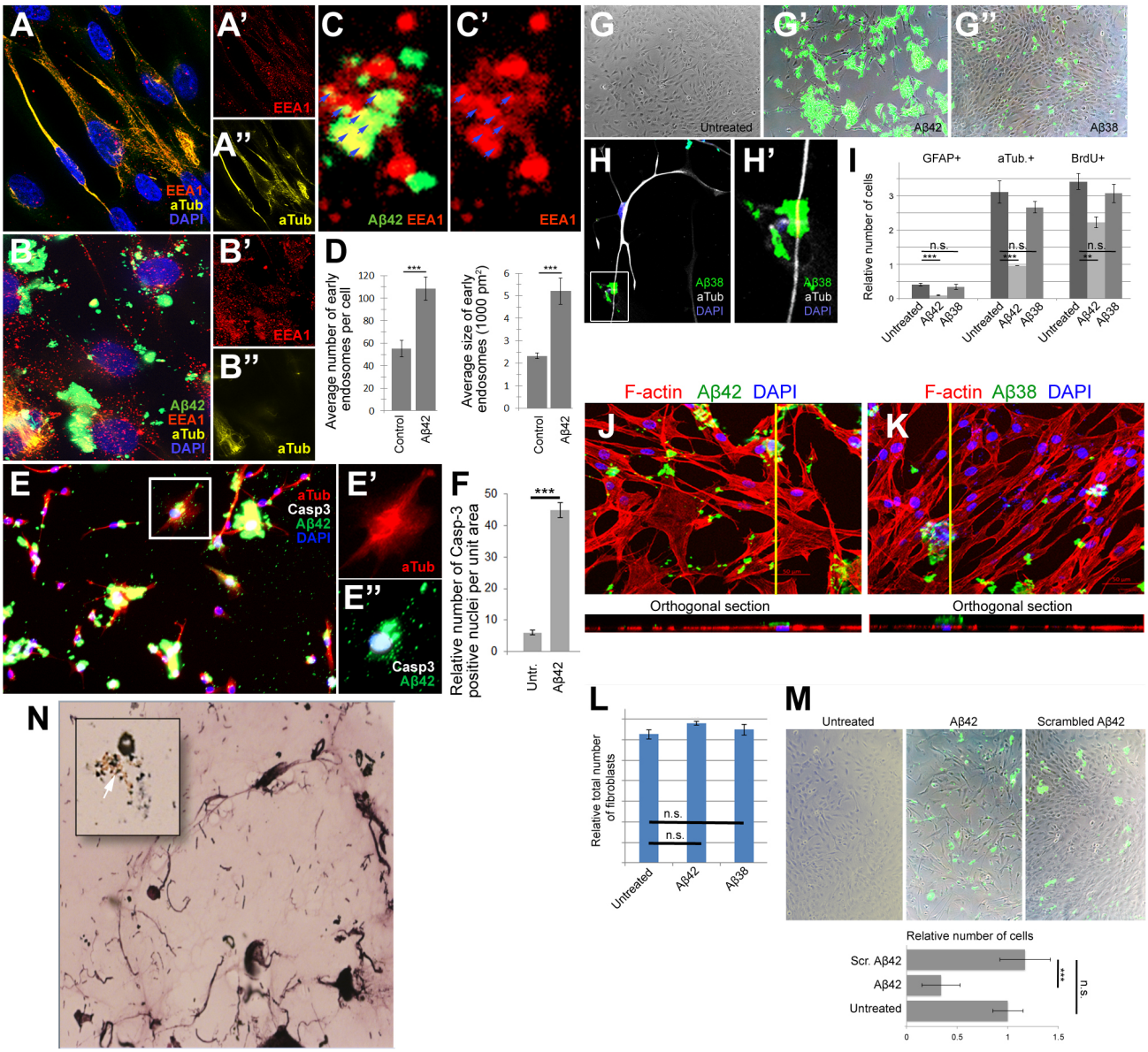

Figure S2, related to Figures 3-7
Amyloid aggregation dynamics and control experiments

(A) Immunostaining for acetylated tubulin and early endosomes (EEA1) in control cultures.
(A', A'') Individual fluorescence channels for EEA1 and acetylated tubulin in control cultures.
(B) Immunostaining for acetylated tubulin and early endosomes (EEA1) in Aβ42-treated cultures.
(B', B'') Individual fluorescence channels for EEA1 and acetylated tubulin in Aβ42-treated PHCCs.
(C, C') Co-localization of EEA1 and Aβ42.
(D) Quantification of the average number of early endosomes per cell and the average size of early endosomes per cell in control and Aβ42-treated cultures.
(E) Immunostaining of Aβ42-treated cells for acetylated tubulin (red), Aβ42 (green) and caspase-3 (white).
(E') Individual fluorescence channel for acetylated tubulin.
(E'') Fluorescence channels for Aβ42 and Caspase-3.
(F) Quantification of Caspase-3-positive cells in control and Aβ42-treated cultures.

(G) Bright field image of control cultures.
(G') Bright field image of Aβ42-treated cultures.
(G'') Bright field image of Aβ38-treated cultures.
(H) Confocal image of acetylated tubulin immunostaining on Aβ38-treated cultures.
(H') Close-up of a region from H showing cells treated with Aβ38.
(I) Quantification of the relative number of untreated, Aβ42-treated and Aβ38-treated cells immunoreactive for GFAP, acetylated tubulin or BrdU.
(J) Confocal image over the *z*-axis and orthogonal section over the *y*-axis of Aβ42-treated human-derived fibroblasts. F-actin was stained with phalloidin, and DNA was stained with DAPI.
(K) Confocal image over the *z*-axis and orthogonal section over the *y*-axis of Aβ38-treated human-derived fibroblasts. F-actin was stained with phalloidin, and DNA was stained with DAPI.
(L) Quantification of the relative total number of fibroblasts in control, Aβ42-treated and Aβ38-treated samples.
(M) Bright field image of control, Aβ42-treated, and scrambled Aβ42-treated cultures, and quantification of relative cell numbers.
(N) Gallyas silver impregnation staining for neurofibrillary tangles in 3D cultures. Inset shows the senile plaques (white arrow).
Scale bars 20 μm.

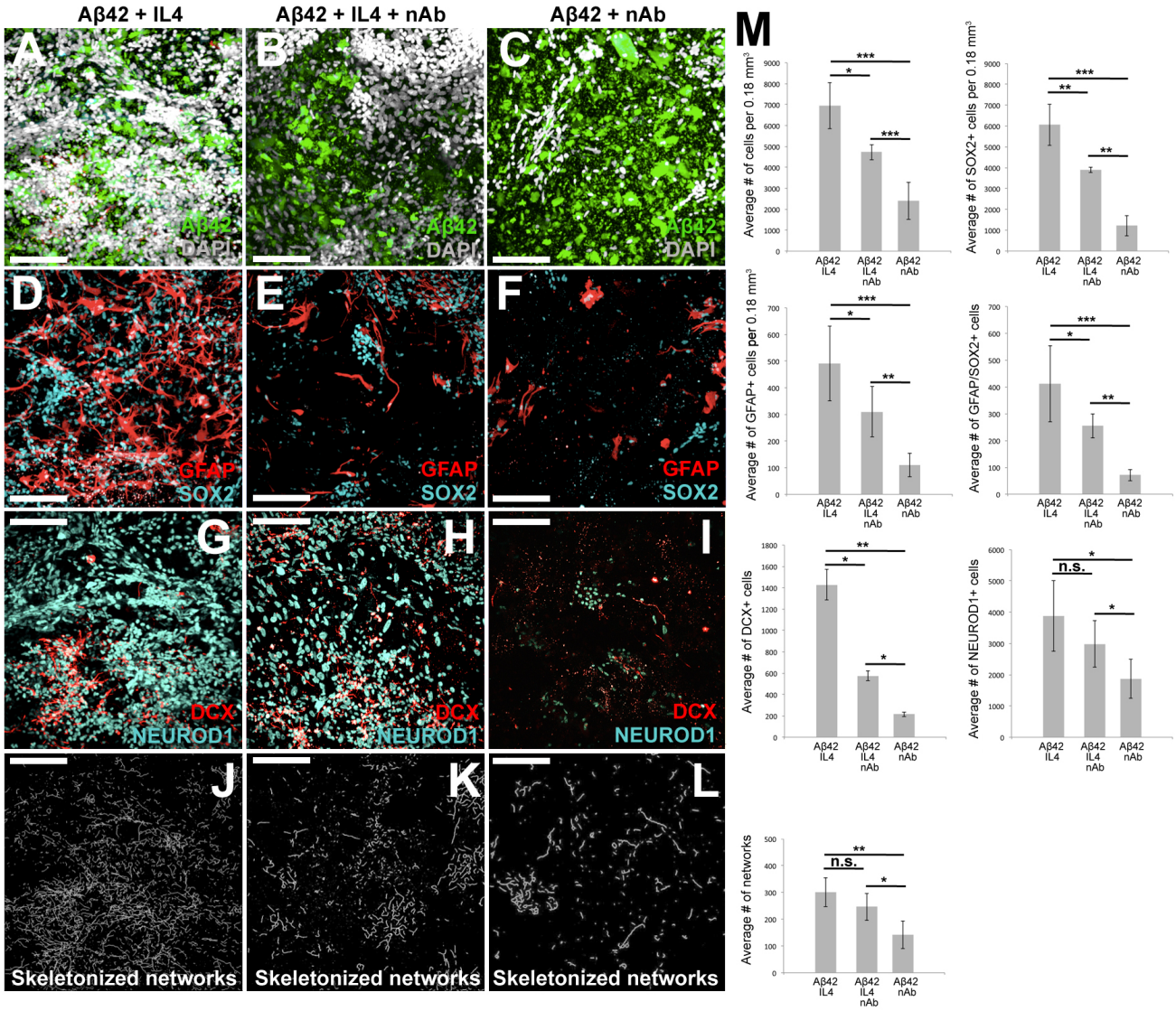

Figure S3, related to Figures 5 and 6

The rescue effect of Interleukin-4 is specific.

(A-C) Aβ42 and DAPI in Aβ42+IL4-treated (A), Aβ42 + IL4 + neutralizing IL4 antibody (nAb)-treated (B), and Aβ42 + nAb-treated gels (C).

(D-F) GFAP and SOX2 in Aβ42+IL4-treated (D), Aβ42 + IL4 + nAb-treated (E), and Aβ42 + nAb-treated gels (F).

(G-I) DCX and NEUROD1 in Aβ42+IL4-treated (G), Aβ42 + IL4 + nAb-treated (H), and Aβ42 + nAb-treated gels (I).

(J-L) Skeletonized networks of connected paths in Aβ42+IL4-treated (J), Aβ42 + IL4 + nAb-treated (K), and Aβ42 + nAb-treated gels (L).

(M) Quantifications of A-L.

Scale bars: 100 μm. All gels are 3 weeks of culture.

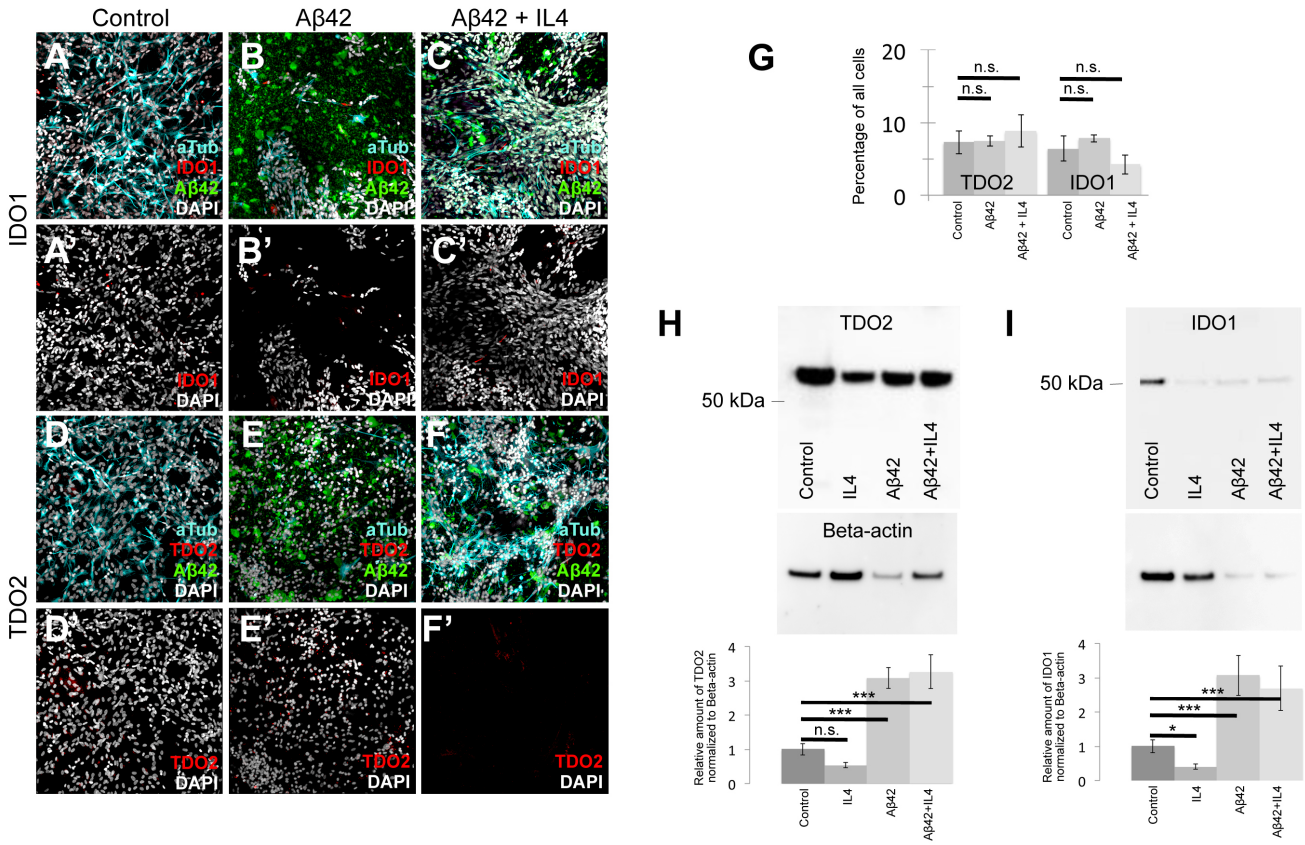

Figure S4, related to Figure 6
Expression of TDO2 and IDO1.
(A-C) Acetylated tubulin, IDO1 and Aβ42 in control (A), Aβ42-treated (B), Aβ42 + IL4-treated gels (C).
(A'-C') IDO1 and DAPI channels of A-C, respectively.
(D-F) Acetylated tubulin, TDO2 and Aβ42 in control (D), Aβ42-treated (E), Aβ42 + IL4-treated gels (F).
(D'-F') TDO2 and DAPI channels of D-F, respectively.
(G) Quantification graph of the percentage of cells expressing TDO2 or IDO1 in A-F'.
(H) Western blot and quantification graph for TDO2.
(I) Western blot and quantification graph for IDO2.
Scale bars: 100 μm. All gels are 3 weeks of culture.

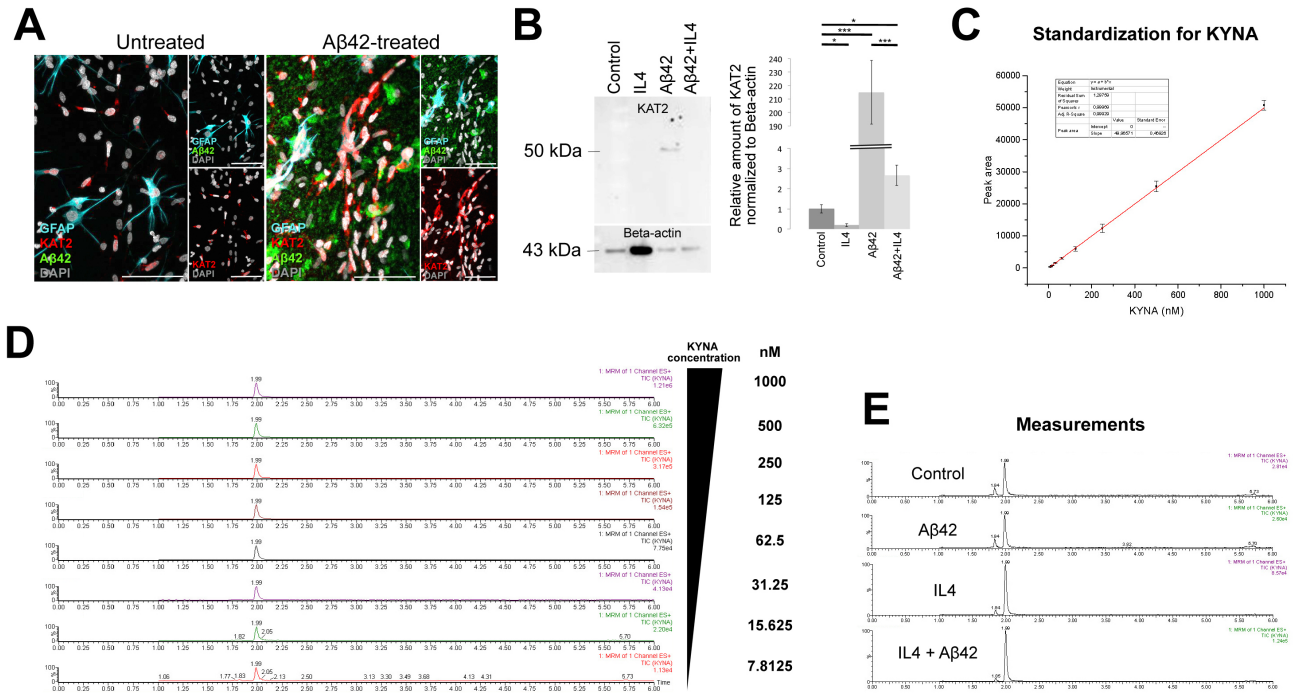

Figure S5, related to Figure 6
Measurement of KYNA concentrations.

(A) Immunocytochemical staining for GFAP (cyan), KAT2 (red), and Aβ42 (green) in untreated and Aβ42-treated gels. Small panels are individual combinations of fluorescence channels.

(B) Western blot for KAT2.

(C) Calibration curve for various concentrations of KYNA.

(D) Liquid chromatography-mass spectroscopy (LC-MS/MS) running curves for different KYNA concentrations.

(E) LC-MS/MS running curves for untreated (control), Aβ42-treated, IL4-treated, and Aβ42+IL4-treated gels.

Scale bars: 50 μm. All gels are 3 weeks of culture.

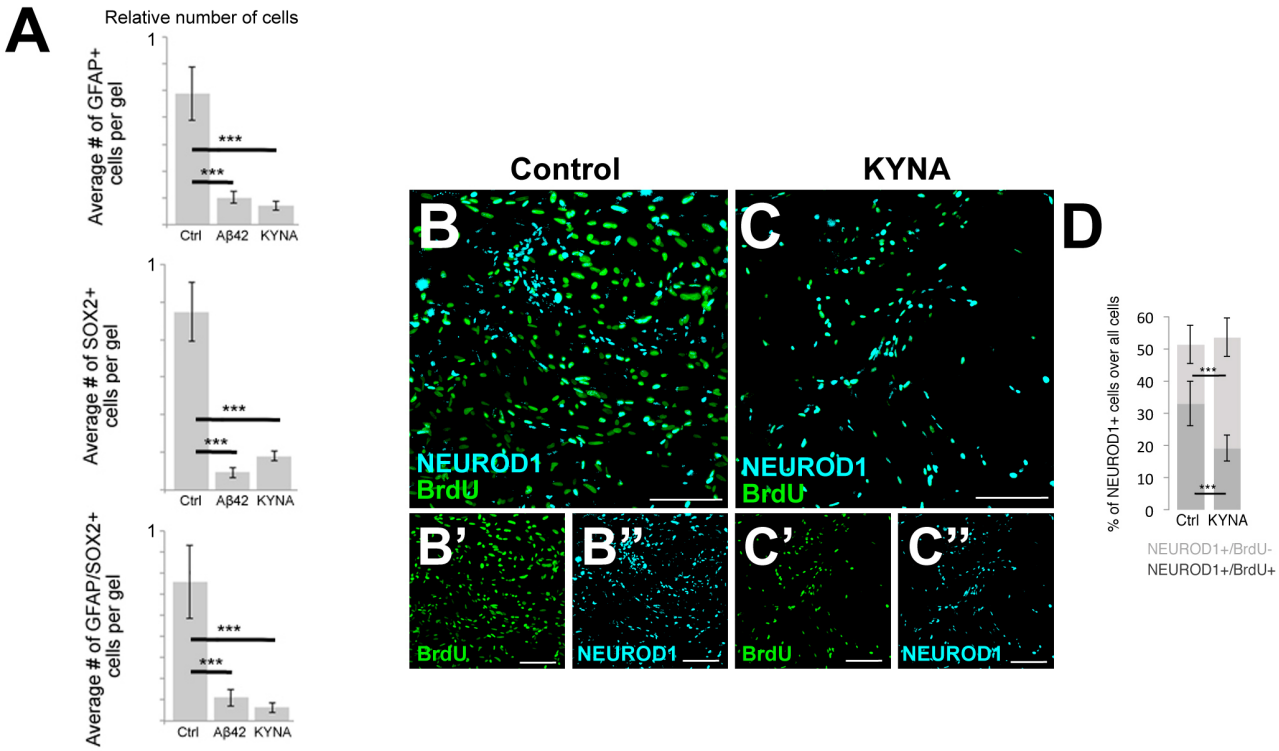

Figure S6, related to Figures 5 and 6
The effects of Kynurenic acid on neurogenic capacity and proliferative ability.
(A) Quantification graphs for the number of GFAP+/SOX2-, GFAP-/SOX2+ and GFAP+/SOX2+ progenitors in control, Aβ42-treated and KYNA-treated gels.
(B, C'') NEUROD1 and BrdU in control (B) and Kynurenic acid (KYNA)-treated gels (C). Smaller images under the panels are single fluorescent images (B', B'', C', C'').
(D) Quantification graph for B-C''.
Scale bars: 100 μm. All gels are 3 weeks of culture.